Evaluating and improving wave and non-wave stress parametrisations for oceanic flows

Daniel R. Johnston,[a,b]   Callum J. Shakespeare,[b]   and Navid C. Constantinou,[c,d]

[a] *School of Science, UNSW Canberra, Australia*
[b] *Research School of Earth Sciences, Australian National University, Australia*
[c] *School of Geography, Earth and Atmospheric Sciences, University of Melbourne, Australia*
[d] *Australian Research Council Centre of Excellence for the Weather of the 21st Century, University of Melbourne, Australia*

ABSTRACT: Whenever oceanic currents flow over rough topography, there is an associated stress that acts to modify the flow. In the deep ocean, this stress is predominantly a form drag due to pressure differentials across topography, caused by the formation of internal waves and other baroclinic motions: processes that act on such small scales most global ocean models cannot resolve. Despite the need to incorporate this stress into ocean models, existing parametrisations are limited in their applicability. For instance, most parametrisations are only suitable for small-scale topography and are either for periodic or steady flows, but rarely a combination thereof. Here we summarise some of the most widely used parametrisations and evaluate the accuracy of a carefully selected subset using hundreds of idealised two-dimensional and three-dimensional simulations spanning a wide parameter space. We focus on the case of an isolated Gaussian hill as an idealised representation of a seamount. In cases where the parametrisations prove to be inaccurate, we use our data to suggest improved formulations. Our results thus provide a starting point for a comprehensive parameterisation of topographic stresses in ocean models where fine scale topography is unresolved.

SIGNIFICANCE STATEMENT: As the ocean flows over topographic features it experiences a force. Such topography includes undersea mountains that are too small to be accurately described by global ocean and climate models. These forces shape the ocean structure considerably and affect large-scale ocean circulation features, like the Atlantic Meridional Overturning Circulation. Because there is no hope to accurately include these small-scale effects in climate projections we need expressions (a.k.a. parametrisations) for the collective force they exert on the ocean. Here, we evaluate existing parametrisations for the force created when an oceanic current flows over an underwater hill by comparing them to the output of small-scale, high-resolution ocean simulations. Compared to previous studies, we cover a much wider range of cases. This allows us to see where existing parametrisations break down and also suggest improvements to these parametrisations, taking us closer to the goal of developing a general and widely applicable mathematical description of this phenomenon.

1. Introduction

In shallow seas, fast moving currents are subject to significant energy losses from frictional drag along the ocean bottom. However in the deep ocean, where currents are slower, there is still a significant amount of energy dissipation attributed to the formation of internal waves in regions of rough topography (Ledwell et al. 2000; Egbert and Ray 2000, 2001; Naveira Garabato et al. 2013). These waves can cause substantial mixing, which plays a role in nutrient

transport and large scale ocean circulation (Sandstrom and Elliott 1984; Munk and Wunsch 1998; Melet et al. 2013, 2014).

Over half of the ocean floor is covered by abyssal hills and mountains, defined respectively as having a variation in height of $300 - 1000$ m and greater than 1000 m (Harris et al. 2014) over a 750 arc second (or $\approx 10 - 20$ km) radius. Since internal waves generated at these features are of a comparable horizontal scale to the topography itself (e.g., Llewellyn Smith and Young 2002), resolving these waves is not possible with current global ocean models which generally have horizontal resolutions on the order of 10 to 100 km (e.g., Ansong et al. 2015; Kiss et al. 2020). As a result, it is important to have parametrisations for the effects of internal waves generated at such hills. Existing parametrisations have mainly focused on computing the energy flux extracted from the flow due to the generation of internal waves (e.g., Simmons et al. 2004; Jayne 2009; Olbers and Eden 2013; de Lavergne et al. 2019). Such a focus is justified, as it has allowed better understanding of the contribution of internal waves to tidal and eddy dissipation, and ocean mixing. However, in recent times, there have been further efforts (e.g., Shakespeare et al. 2020; Klymak et al. 2021; Eden et al. 2021) which attempt to develop parametrisations for the corresponding topographic stress due to internal waves and other related effects. These effects include blocking (Winters and Armi 2014; Nikurashin et al. 2014) and bottom-trapped tides formed at high latitudes where a stronger Coriolis force prevents internal waves from freely propagating (Falahat and Nycander 2015; Shakespeare et al. 2020). Developing these stress parametrisations is vital to obtaining accurate

Corresponding author: Daniel R. Johnston, daniel.johnston@unsw.edu.au

representations of eddies and tides, and large-scale flow features such as the Antarctic Circumpolar Current (e.g., Naveira Garabato et al. 2013; Arbic et al. 2019).

To be precise, the energy loss from a spatially uniform flow $\overline{u}$ and topographic stress τ is equal to $\overline{u} \cdot \tau$, and the topographic stress also acts to modify $\overline{u}$. Thus, the topographical stress is a more fundamental quantity to study, in that it can be used to compute energy loss, but this is not necessarily true the other way around. This is particularly the case when $\overline{u}$ is time-varying, so that it is not at all valid to use expressions for the time-averaged energy flux to understand the stress τ. Doing so omits any component of the stress τ that is out-of-phase with the flow $\overline{u}$, which in some cases is the entire stress (e.g., for bottom-trapped tides; Falahat and Nycander 2015; Shakespeare et al. 2020)

Due to the complexity of developing a generic parametrisation for stress, existing work (e.g., Bell 1975; Jayne and St. Laurent 2001; Klymak et al. 2010; Shakespeare et al. 2020) has focused on special cases. For instance, previous studies have treated steady and tidal flows in isolation. However, since the steady and tidal components of a flow can interact (Shakespeare 2020), it is important for existing parametrisations to be extended to mixed flows. Existing parametrisations also have several other assumptions that can reduce their accuracy if incorporated into ocean models. For example, it is often assumed that the topography height is small (Bell 1975; Shakespeare et al. 2020) or that the latitude is close to 0° (Jayne and St. Laurent 2001; Klymak et al. 2010).

The first goal of this paper is to evaluate the accuracy of a subset of available wave and non-wave stress parametrisations. This is done by comparing theoretical expressions to the stress calculated from a large suite of ocean simulations. The main parametrisations we focus on are those due to Bell (1975), Jayne and St. Laurent (2001), Klymak et al. (2010) and Shakespeare et al. (2020), and we refer to the reader to other related works throughout. Here we focus on the magnitude of the stress the fluid exerts on the topography, rather than discerning exactly where in the water column the equal and opposite reaction stress on the ocean is applied. We also focus on the case of an isolated Gaussian hill in either two or three dimensions, which is a standard, simple case which has been studied in the context of related phenomena (Legg and Huijts 2006; Maitland-Davies and Bühler 2025). A Gaussian hill is a decent model for an isolated undersea mountain (seamount). However, a stronger motivation in this case is that working with isolated hills means that there are only a small number of well-defined parameters to consider (i.e., height and width), allowing us to ensure that the basic physics and scalings of the parametrisations are correct. This is in contrast to other studies (e.g., Jayne and St. Laurent 2001; Buijsman et al. 2015; Shakespeare et al. 2021a) which tend to only test stress parametrisations with global models or more complicated topography,

and often with more limited parameter regimes. In a similar vein, we reduce the complexity of our simulations by taking the stratification to be constant. We also note that whilst three-dimensional simulations are more physically realistic, they are more computationally expensive than two-dimensional simulations. Moreover, two-dimensional topography may be interpreted as approximating a section of a three-dimensional ridge, which can be sites of significant internal wave generation (Ledwell et al. 2000; Garrett and Kunze 2007). Two-dimensional simulations are thus useful despite being less broadly applicable than three-dimensional models. As a result, our general procedure is to run a large number of tests in two dimensions, and then further analyse any interesting phenomena in three dimensions.

The second goal of this paper is to suggest improvements to existing stress parametrisations. This is done using predominantly mathematical or physical arguments that are supported by the simulation data. Notably, one of the common shortcomings in existing parametrisations is the assumption of small topographic height despite tall topographic features being abundant in the ocean (Harris et al. 2014). Moreover, large isolated seamounts are of interest in ecology, vulcanology and ship navigation (Clark et al. 2010; Watts 2019). Therefore, it is important for existing parametrisations to be extended to such cases. The ultimate goal of this work is to understand the isolated hill regime in detail and help pave the way for a more complete parametrisation of wave and non-wave stress for implementation in global ocean models.

The structure of the paper is as follows. In Section 2 we recall some existing drag parametrisations used for tidal, steady and mixed flows. In Section 3 we discuss the setup for our simulations. In Section 4 we then discuss the results of the simulations, and use these results to evaluate and suggest improvements to each parametrisation. Finally, in Section 5 we discuss the main takeaways from our analysis, and describe a combined parametrisation that depends on the type of flow and scale of topography under consideration.

2. Existing parametrisations

We begin by summarising existing parametrisations for wave and non-wave stress. The parametrisations are categorised depending on the flow under consideration — tidal, steady or mixed. Each parametrisation is expressed in its general form, but we also simplify for the case of an isolated Gaussian hill. For a two-dimensional domain (viewed as cross-section of three-dimensional space) with horizontal component $[-L_x/2, L_x/2]$, we define the stress as

$$F_{2\mathrm{d}} = \frac{1}{\rho_0} \int_{-L_x/2}^{L_x/2} p_h \frac{\mathrm{d}h}{\mathrm{d}x} \mathrm{d}x, \qquad (1)$$

where $h(x)$ is the bottom topography, $p_h(x)$ the bottom pressure, and ρ_0 is the background density of the sea water. In particular, the stress (1) is the net force per spanwise unit length created from the pressure differential across the hill, divided by ρ_0 for convenience. As a result, F_{2d} has units $N\,m^2\,kg^{-1}$ and $\rho_0 F_{2d}$ has units of force per unit length. The sign of F_{2d} is also such that a positive value of F_{2d} corresponds to a force per unit length of magnitude $|\rho_0 F_{2d}|$ acting on the hill in the positive x-direction, along with an equal and opposite force acting on the flow in the negative x-direction. In three dimensions, with a horizontal domain $[-L_x/2, L_x/2] \times [-L_y/2, L_y/2]$, we then define the stress due to a topography $h(x, y)$ as the vector

$$\boldsymbol{F}_{3d} = \frac{1}{\rho_0} \int_{-L_y/2}^{L_y/2} \int_{-L_x/2}^{L_x/2} p_h \boldsymbol{\nabla} h \, \mathrm{d}x \mathrm{d}y. \qquad (2)$$

Note that $\boldsymbol{F}_{3d}$ has units $N\,m^3\,kg^{-1}$ and $\rho_0 \boldsymbol{F}_{3d}$ has units of force.

In what follows, our domain is as shown in Figure 1, with dimensions $L_x \times L_y \times H$ and a spatially mean zonal flow $U(t)$ over topography $h(x, y)$. For two-dimensional analysis, we restrict ourselves to the x–z plane. Moreover, for the ensuing theoretical analysis in this section, we assume L_x and L_y are large. That is, $L_x, L_y \to \infty$.

Throughout this paper, we use the closely related terms "stress" and "internal wave drag". To avoid any confusion, we briefly clarify what is meant by each of these terms. By "stress", or more correctly "form stress", we mean the total force (scaled by $1/\rho_0$) acting on the flow as per (1) or (2). "Internal wave drag" refers to the component of form stress due to the formation of internal waves. Many existing parametrisations focus only on internal wave drag, which is the dominant component of stress in many idealised scenarios, but not if the flow is blocked or sufficiently non-linear.

a. Case 1: Tidal Flow

We consider a periodic tidal flow $U(t) = U_{\text{tidal}} \cos(\omega t)$ in the x-direction where U_{tidal} is a constant and ω is the tidal frequency. Tidal flows are a major source of internal waves and the stress associated with their generation impacts the strength of both barotropic and internal tides (Ansong et al. 2015; Buijsman et al. 2015). As a result, this flow regime is the main focus in the oceanic literature.

In the work of Bell (1975), linear theory was used to develop an expression for the energy flux generated by internal tidal waves. Bell found his theory to compare favorably with observations, and his parametrisations have since been refined by others including Llewellyn Smith and Young (2002), Khatiwala (2003) and Nycander (2005). Although Bell's theory was derived for small-scale topography, recent work (Geoffroy et al. 2024; Pollmann and

Nycander 2023) suggests that Bell's linear theory can still be reliable for moderately large topography, particularly for low mode waves. However, because Bell's parametrisation and its derivatives provide expressions for the time-averaged energy flux, they cannot be directly converted to time-dependent stress parametrisations.

For our analysis, we focus on two easily applied stress parametrisations closely related to the work of Bell (1975). First, we will discuss an older and ubiquitously applied parametrisation due to Jayne and St. Laurent (2001, hereafter, JSL2001), which is essentially a scaling for stress based on Bell's formula for the internal tide energy flux. Then, we will analyse a more mathematically rigorous parametrisation due to Shakespeare et al. (2020, hereafter SAH2020). A comparison of other similar parametrisations, with a focus on energy conversion, is given by Green and Nycander (2013).

1) JAYNE AND ST LAURENT PARAMETRISATION

Jayne and St Laurent give a simple estimate for internal wave drag, by assuming that the stress scales in an identical way to the Bell's energy flux formula. Despite the simple form of the JSL2001 parametrisation, it has been shown to significantly improve the accuracy of tidal models when compared to observations, and is widely used today (Arbic et al. 2018; Ansong et al. 2015). For each grid cell, they set the stress (in each horizontal dimension) to be proportional to Nh^2u. Here, N is the buoyancy frequency, and h and u are taken to be suitable values of the topography height and tidal velocity in the grid cell. For small $h \ll H$, we can approximate u as the barotropic flow $U(t)$ and N as a constant in the vicinity of the topography. Thus, the total stress over a small hill with root mean square height h_{rms} is estimated by

$$F_{\text{JSL}} = \frac{1}{2} \kappa N_B h_{rms}^2 U. \qquad (3)$$

Here, κ is the tunable scaling constant in JSL2001, N_B denotes the buoyancy frequency at the seabed, and the subscript "JSL" indicates that this is the drag force due to the JSL2001 theory. In line with our units and scaling for stress in (1) and (2), here κ has units of length in three dimensions and is unitless in two dimensions. On the other hand, in JSL2001 the stress is implicitly divided by the horizontal length (in two-dimensions) or area (in three-dimensions) so that κ has units of inverse length and may therefore be interpreted as the characteristic wavenumber of the topography. Note that the factor of $1/2$ in (3) could be absorbed into the definition of κ, but we have included it to more closely match the expression given by JSL2001.

Although simple and widely used, there are some notable limitations of the JSL2001 model. Firstly, the model was only designed for small-scale topography and large ocean depths. In addition:
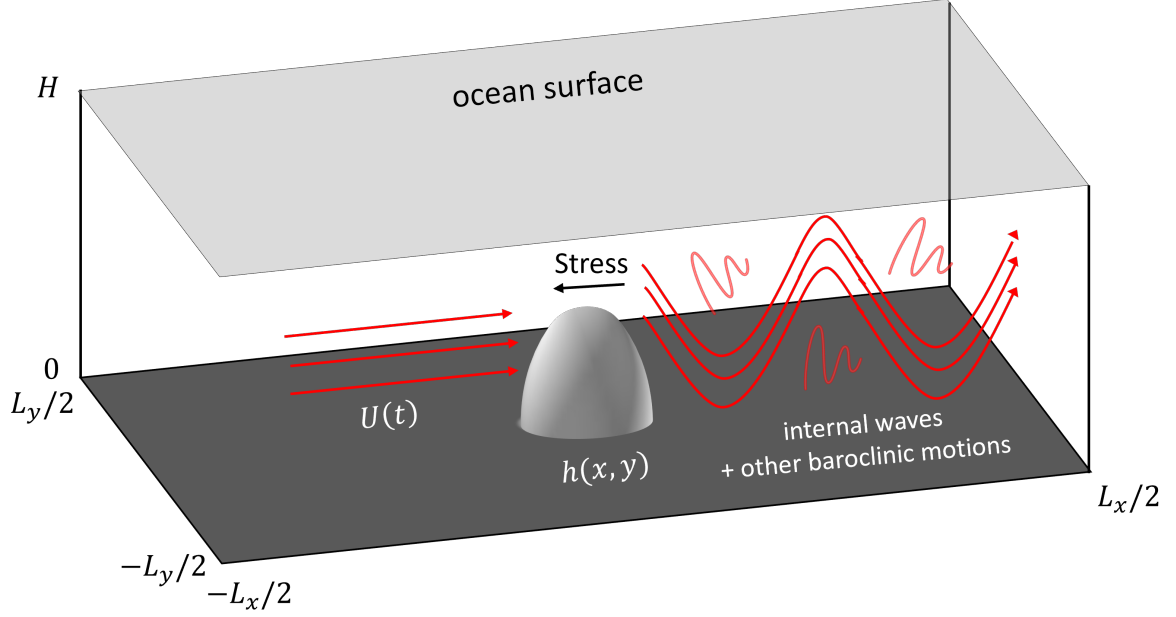
FIG. 1. A schematic of the model domain. A spatially mean flow $U(t)$ interacts with the topography $h(x, y)$ to generate baroclinic motions and an associated stress.

1. Representing a complicated region of topography by a single wavenumber κ is very simplistic and a more sophisticated formulation would be preferred.

2. Using the bottom value of stratification N_B has since been shown to be unreliable, and it is more accurate to use an averaged form of the stratification (Zarroug et al. 2010; Lüschow and Von Storch 2024).

3. The parametrisation (3) is latitude-independent, an omission which Jayne and St Laurent state could be significant when the tidal frequency ω is close to the Coriolis frequency f.

2) SHAKESPEARE, ARBIC AND HOGG PARAMETRISATION

In SAH2020, the authors take a more analytic approach to parametrising tidal flow stress, giving an expression which refines that of JSL2001 (Equation (3)). The main novelty of their work is their treatment of "spring" forces, such as bottom-trapped tides, which are out-of-phase with the tidal flow and so do not do any work in the time mean. This is important, because JSL2001 and other prior parametrisations compute stress via a comparison to the time-averaged energy flux, and thus do not account for such spring forces. Since the parametrisation of SAH2020 refines that of JSL2001, including by adding frequency dependence (point 3 above) and a more sophisticated representation of the topographic spectrum (1 above), we mainly compare our numerical simulations with the SAH2020 theory, whilst commenting on the limitations of the JSL2001 theory.

Under standard assumptions, including small topographic height and large ocean depth, SAH2020 give the stress for subcritical latitudes ($|f| < \omega$) and isotropic topography as

$$F_{3d} = \frac{\sqrt{(N^2 - \alpha\omega^2)(\omega^2 - f^2)}}{4\pi|\omega|} U \int_0^\infty |\hat{h}(K)|^2 K^2 dK. \quad (4)$$

Here, $\alpha \in \{0, 1\}$ is such that

$$\alpha = \begin{cases} 0, & \text{under the hydrostatic assumption,} \\ 1, & \text{otherwise.} \end{cases} \quad (5)$$

Then, $\hat{h}$ denotes the Fourier transform of h in t, x and y to transformed variables ω, k and ℓ respectively with $K \stackrel{\text{def}}{=} \sqrt{k^2 + \ell^2}$. Note that we use the Fourier transform convention

$$\hat{g}(k) \stackrel{\text{def}}{=} \int_{-\infty}^\infty g(x) e^{-ikx} dx. \quad (6)$$

Since we are assuming the topography is isotropic (and independent of time), $\hat{h}$ is a function of the total wavenumber K only, as indicated in (4). We also remark that (4) is only the x-component of the stress, as this is the primary direction of our flow and focus of our analysis.

As a direct comparison to the JSL2001 parametrisation, a clear frequency dependency has been added and the con-

stant κ in (3) has been replaced with the analytic expression

$$\frac{1}{2\pi h_{\mathrm{rms}}^2} \int_0^\infty |\hat{h}(K)|^2 K^2 \mathrm{d}K.$$

In particular, in the limit where $N \gg \omega \gg f$, F_{3d} reduces exactly to the JSL2001 expression (3), albeit with an analytic expression for what κ should be set to.

In SAH2020, a more general expression than (4) is stated which accounts for wave reflections off the ocean surface. However, such reflections are difficult to parametrise (e.g., Shakespeare et al. 2021b), and for a narrow, isolated hill in a deep ocean the number of waves reflecting back onto the topography is small. Therefore, we omit any reflection terms from (4) for simplicity. Nevertheless, we note that these reflections become important even for an isolated hill when the half-vertical wavelength λ_v compared to the ocean depth H, known as the mode-number

$$n = \frac{H}{\lambda_v/2} = \frac{KH\sqrt{N^2 - \alpha\omega^2}}{\pi\sqrt{\omega^2 - f^2}}, \tag{7}$$

approaches 1 (from above). As a result, we expect (4) may have deviations from the actual stress for small K, H or N.

In the case of an isolated Gaussian hill with width W, whereby

$$h(x, y) = h_0 e^{-(x^2+y^2)/(2W^2)} \tag{8}$$

we obtain from (4)

$$F_{3d} = \frac{\pi\sqrt{\pi}}{4} W \frac{\sqrt{(N^2 - \alpha\omega^2)(\omega^2 - f^2)}}{\omega} h_0^2 U. \tag{9}$$

Importantly, (9) suggests that the stress depends linearly on the hill width W, at least for Gaussian hills.

The expression for supercritical (bottom-trapped) latitudes $|f| \geq \omega$ is similar, but with the stress out of phase with velocity. In particular, for a Gaussian hill

$$F_{\mathrm{SAH3d}} = \frac{\pi\sqrt{\pi}}{4} W \omega^{-1} h_0^2 U_{\mathrm{tidal}} \times$$
$$\times \begin{cases} \sqrt{(N^2 - \alpha\omega^2)(\omega^2 - f^2)} \cos(\omega t), & |f| < \omega, \\ \sqrt{(N^2 - \alpha\omega^2)(f^2 - \omega^2)} \sin(\omega t), & |f| \geq \omega, \end{cases} \tag{10}$$

where the subscript SAH3d indicates that this is the three-dimensional stress due to the SAH2020 theory. In a subsequent paper (Shakespeare et al. 2021a), the authors also give a parametrisation for two dimensions. Namely, for a Gaussian hill $h(x) = h_0 e^{-x^2/(2W^2)}$,

$$F_{\mathrm{SAH2d}} = \omega^{-1} h_0^2 U_{\mathrm{tidal}} \times$$
$$\times \begin{cases} \sqrt{(N^2 - \alpha\omega^2)(\omega^2 - f^2)} \cos(\omega t), & |f| < \omega, \\ \sqrt{(N^2 - \alpha\omega^2)(f^2 - \omega^2)} \sin(\omega t), & |f| \geq \omega. \end{cases} \tag{11}$$

Note that (11) is identical to (10) except without the factor of $\pi\sqrt{\pi}W/4$. To obtain (10) and (11) one also needs to assume that N is constant, which we will do throughout our analysis. As discussed before, in the more physical setting where N is varying function of depth, it is better to use an averaged value of N, at least for sufficiently large hill widths (Lüschow and Von Storch 2024).

b. *Case 2: Steady Flow*

We now consider a constant steady flow U in the x-direction. Under such a flow, the internal waves formed are called lee waves. These lee waves have zero Eulerian frequency (i.e., are steady at a fixed point), and are formed with intrinsic frequency depending on the topography and the magnitude of U. This leads to some added complexities compared to the tidal case, where the internal waves have the same intrinsic frequency as the tide. In particular, for steady flows there is a greater dependency on the Froude number

$$Fr \stackrel{\mathrm{def}}{=} \frac{Nh}{U}. \tag{12}$$

For large Froude numbers, the system becomes highly non-linear and harder to parametrise. Namely, when $Fr \gtrsim 1$, this non-linearity manifests as blocking or splitting, which can significantly decrease the formation of lee waves (Nikurashin et al. 2014).

As in the tidal case, we also focus on two parametrisations for steady flows, treating the cases of small and large Froude numbers separately. The first, which is based on the linear theory of Bell (1975), is an idealised theory assuming lee waves form without the effects of a high Froude number. The second, is a semi-empirical parametrisation due to Klymak et al. (2010, hereafter, KLP2010). The KLP2010 parametrisation focuses instead on a regime where most of the flow is blocked, and unable to surmount the topography to form lee waves. These two parametrisations therefore look at different aspects of the wave and non-wave stress, and so both are useful in obtaining a wholistic parametrisation. Of course, there is also the transitional case where Froude number is of a moderate size, say $Fr \approx 1 - 10$. To limit the scope of our analysis we do not explore this case in depth here, but refer the reader to recent attempts at developing a hybrid parametrisation (Perfect et al. 2020; Klymak et al. 2021; Baker and Mashayek 2022).

1) BELL PARAMETRISATION FOR STEADY FLOWS

In the work of Bell (1975), an expression for the time-mean stress due to lee waves is provided. In three dimen-

sions, his expression for the x-component of stress is

$$F_{\text{Bell3d}} =$$
$$= \frac{1}{4\pi^2} \iint \frac{k\,|\hat{h}(k,\ell)|^2}{\sqrt{k^2+\ell^2}} \sqrt{[N^2-\alpha(kU)^2][(kU)^2-f^2]}\mathrm{d}k\mathrm{d}\ell \tag{13}$$

where α is as in (5) and the integrals are taken over all real values of k and ℓ under the restriction $|f| \leq |kU| < \infty$ for hydrostatic ($\alpha = 0$) and $|f| \leq |kU| \leq N$ for non-hydrostatic ($\alpha = 1$) conditions. As we are taking the flow speed to be constant, the lee wave stress is non-zero in the time-mean and there is not an equivalent bottom-trapped spring force as in the SAH2020 tidal parametrisation theory. However, it is worth noting that (13) can readily be obtained by repeating the arguments in SAH2020 for a steady flow. The two-dimensional equivalent of (13) is then

$$F_{\text{Bell2d}} =$$
$$= \frac{1}{2\pi} \int\limits_{\substack{|f| \leq |kU| \\ \alpha|kU| \leq N}} |\hat{h}(k)|^2 \sqrt{[N^2-\alpha(kU)^2][(kU)^2-f^2]}\mathrm{d}k. \tag{14}$$

We now consider the case of an isolated Gaussian hill of height h_0. In general, (13) and (14) do not simplify much further unless one wishes to express the parametrisations in terms of incomplete Bessel functions. However, in the special case at the equator ($f = 0$) with a hydrostatic assumption ($\alpha = 0$), we have

$$F_{\text{Bell3d}}(\alpha = f = 0) = \frac{\pi\sqrt{\pi}}{4} W N h_0^2 U, \tag{15}$$
$$F_{\text{Bell2d}}(\alpha = f = 0) = N h_0^2 U, \tag{16}$$

which is the same as what one obtains in the tidal case (cf. (10) and (11)).

Bell's parametrisations are derived in the case $Fr \ll 1$. For higher Froude numbers the lee wave flux saturates as non-linear blocking and splitting effects take hold (Nikurashin et al. 2014). In more recent energy flux parametrisations (e.g., Baker and Mashayek 2022), a simple scaling is used to account for this phenomena. Namely, let E denote the internal wave energy flux and E_{Bell} denote the energy flux predicted by the Bell (1975) theory. Then for some critical Froude number Fr_c one sets

$$E = \left(\frac{Fr_c}{Fr}\right)^2 E_{\text{Bell}}. \tag{17}$$

whenever $Fr \geq Fr_c$. The standard values of Fr_c used are 0.7 in two dimensions, and 0.4 in three dimensions. These values were derived empirically from experimental

observations (Aguilar and Sutherland 2006) and simulation data (Nikurashin et al. 2014).

2) Klymak, Legg and Pinkel parametrisation

In KLP2010, a form stress parametrisation is obtained for when the Froude number Fr is very large, whereby blocking effects are the dominant form of stress. Their parametrisation is derived using numerical simulations for two-dimensional Gaussian hills under the hydrostatic assumption and $f = 0$. The full expression for the form stress in KLP2010 is

$$F_{\text{KLP}} = N h_0^2 U_m \left[1 + \pi \frac{U_m}{Nh_0} - 2\pi^2 \left(\frac{U_m}{Nh_0}\right)^2 \right] \tag{18}$$

where h_0 is the hill height and

$$U_m = \frac{H}{H-h_0} U. \tag{19}$$

In KLP2010, a factor of $\pi/2$ actually appears out the front of (18). However, this is the result of a small algebraic error so that the factor is actually $\pi/3 \approx 1$.

For $Fr \gg 1$, the second and third terms in (18) are small, so that this parametrisation is nearly equivalent to the linear lee wave stress given in (16). The main difference is the scaling of U by $H/(H-h)$, which represents the increase in velocity as the flow moves over the narrower channel above the hill. This suggests that when $f = 0$, an approximate $Nh_0^2 U$ scaling could be accurate for both low and high Froude numbers.

To limit the scope of this paper we focus on the cases $Fr \ll 1$ (Bell (1975) theory) and $Fr \gg 1$ (KLP2010 theory) discussed above. However, there are also intermediate regimes $Fr \approx 1$ that one can consider. In this regard, "hybrid" parametrisations have been developed in both the atmospheric (Garner 2005; Lott and Miller 1997) and oceanic (Klymak et al. 2021; Perfect et al. 2020) literature. This style of parametrisation has been successfully compared with both global models (Trossman et al. 2013, 2016) and observations (Trossman. et al. 2015). Such parametrisations generally represent the stress as the sum of a propagating (wave) component near the crest of the topography, and a non-propagating (blocked) component at the base of the topography.

c. Case 3: Mixed Flow

Finally, we consider a mixed flow in the x-direction of the form

$$U(t) = U_{\text{mean}} + U_{\text{tidal}} \cos(\omega t), \tag{20}$$

where U_{mean} and U_{tidal} are constants. Compared to the tidal and steady cases, very little work has been done on mixed flows. We thus hope that our subsequent simulations can shine a light on previously unconsidered regimes.

A priori, we expect that the stress for a mixed flow should have a mean (F_m) and periodic (F_P) component i.e.

$$F_{3d} = F_m + F_p \cos(\omega t + \phi) \qquad (21)$$

where ϕ denotes a phase shift. A naive parametrisation would be to assume that the mean (steady) and tidal components of the flow do not interact (although we know this is not the case; e.g., Shakespeare 2020). Nonetheless, if we assume that F_m is independent of U_{tidal} and F_P is independent of U_{mean}, then F_m and F_P can be directly computed from the parametrisations in the steady and tidal cases respectively. There does not appear to be any well-developed parametrisation for F_p in the literature (Bell 1975; Shakespeare 2020, only consider the energy flux), so we primarily compare our simulation data to this naive parametrisation for F_p. Certainly though, one should expect some impact of the mean flow on the periodic stress given that the mean flow will act to Doppler shift the tidal frequency. For the mean component F_m however, there is some existing theory available, which we now discuss.

BELL PARAMETRISATION FOR MIXED FLOWS

Although we previously discussed the Bell (1975) theory for steady flows, Bell also gives a more general expression for the mean stress in mixed flows. Shakespeare (2020) extended this expression to include multiple tidal frequencies, but we will only consider the simpler Bell formulation here. In three dimensions, Bell gives the following formula for the x-component of the time-mean stress (cf. (13))

$$F_{m,\text{3d}} =$$
$$= \frac{1}{4\pi^2} \sum_{n=-\infty}^{\infty} \iint \frac{k \, |\hat{h}(k,\ell)|^2}{\sqrt{k^2+\ell^2}} \sqrt{(N^2 - \alpha\omega_n^2)(\omega_n^2 - f^2)} \times$$
$$\times J_n^2 \left(\frac{kU_{\text{tidal}}}{\omega} \right) dk d\ell, \qquad (22)$$

where $\omega_n = n\omega + kU_{\text{mean}}$, J_n is the nth-order Bessel function of the first kind, and the integrals are taken over all real values of k and ℓ under the restriction $|f| \leq |\omega_n| < \infty$ if $\alpha = 0$ and $|f| \leq |\omega_n| \leq N$ if $\alpha = 1$. The two-dimensional equivalent, which we denote $F_{m,\text{2d}}$ is then given by

$$F_{m,\text{2d}} =$$
$$= \frac{1}{2\pi} \sum_{n=-\infty}^{\infty} \int_{\substack{|f| \leq |\omega_n| \\ \alpha|\omega_n| \leq N}} |\hat{h}(k)|^2 \sqrt{(N^2 - \alpha\omega_n^2)(\omega_n^2 - f^2)} \times$$
$$\times J_n^2 \left(\frac{kU_{\text{tidal}}}{\omega} \right) dk. \qquad (23)$$

There are some notable features of (22). Firstly, if $U_{tidal} = 0$ then (22) reduces to the same expression in the steady flow case (14). Moreover, if $U_{mean} = 0$, we have

$F_{m,\text{3d}} = F_{m,\text{2d}} = 0$. We also note that, provided x is not too large, $J_0(x)$ decreases from 1 whilst $J_n(x)$ increases from 0 for $n \geq 1$. This can be interpreted as the lee wave energy ($n = 0$) being transferred to higher modes ($n \geq 1$) in the presence of a tidal flow (Shakespeare 2020). However, in most cases $J_n(x)$ ($n \geq 1$) is sufficiently small so that the time-mean stress predicted by (22) and (23) is not too different from the case of a purely steady flow.

Like the Bell parametrisation for a steady flow, (22) and (23) are derived in the linear regime, where the Froude number is assumed to be small. Thus, for large Froude numbers, where this theory is invalid, we will primarily compare our simulation data to the naive parametrisation which assumes that the tidal and mean components of the flow do not interact.

3. Numerical Model

We use the Julia library *Oceananigans* (Ramadhan et al. 2020; Wagner et al. 2025) to model flow over an isolated Gaussian hill in two or three dimensions. Importantly, the GPU-capability of Oceananigans allows us to run several hundred simulations whilst using only a modest amount of computational resources (see also Silvestri et al. (2025)). In what follows, we focus on the setup in three dimensions, as the two-dimensional simulations are essentially the same but with only one grid cell in the y-direction and improvements in the resolution. For more precise details of the setup see Johnston et al. (2025), which contains the base code used for each simulation.

By default, our domain was set to be $L_x = L_y = 500$ km long and wide, $H = 1.5$ km deep and centred on a symmetric Gaussian hill $h(x,y) = h_0 \, e^{-(x^2+y^2)/(2W^2)}$ with height h_0 and width $W = 5$ km. Our domain was periodic in the horizontal x-y directions, and bounded in the vertical. To capture the features near the hill, the domain grid was stretched to give a horizontal spacing of $\Delta x = \Delta y \approx 700$ m around the hill, smoothly varied to $\Delta x = \Delta y \approx 2100$ m at the edge of the domain. Similarly, the vertical grid spacing was set to be $\Delta z \approx 7.5$ m in the bottom half of the domain, smoothly varied to $\Delta z \approx 22.5$ m near the surface. The uneven bathymetry is implemented in Oceananigans as an immersed boundary.

To keep the hill isolated, we artificially damped wave features at the horizontal boundaries by introducing a "sponge layer" in the horizontal regions $[-L_x/2, -L_x/4]$, $[L_x/4, L_x/2]$, $[-L_y/2, -L_y/4]$ and $[L_y/4, L_y/2]$. The sponge layer, in x, is:

$$\text{sponge}(x) = \frac{1}{2}\text{Erf}\left(\frac{x - L_x/4}{L_x/16}\right) + \frac{1}{2}\text{Erf}\left(\frac{-x - L_x/4}{L_x/16}\right) + 1, \qquad (24)$$

and similarly in the y-direction for three-dimensional simulations. The sponge region includes a combination of

enhanced explicit horizontal diffusivity and horizontal viscosity (peaking at 2000 m^{2}s^{-1} in the outer regions of the domain) and a relaxation of both buoyancy and horizontal velocity to the background state at a rate of $1/(1.38$ days). To verify that the position of the sponge layer did not affect our results, we also ran initial tests (not shown) with a wider domain, and found negligible change in the output. Implicit dissipation of grid-scale kinetic energy is provided by the advection scheme used, which is an upwind-biased, nominally 9th-order Weighted, Essentially Non-Oscillatory advection scheme, commonly known as WENO (Pressel et al. 2017; Shu 2020; Silvestri et al. 2024).

For each simulation, we specified constant values for background stratification (N), hill height (h_0), hill width (W), ocean depth (H), Coriolis frequency (f), and tidal frequency (ω) if required. Depending on whether we were concerned with a tidal, mean or mixed case, we also specified the flow speeds U_{mean} and U_{tidal} (see (20)). The velocity is initialised as

$$\boldsymbol{u}(t=0) = (U_{\text{mean}} + U_{\text{tidal}})\hat{\boldsymbol{x}}, \qquad (25)$$

and buoyancy is initialised with a linear constant stratification:

$$b(t=0) = N^2 z. \qquad (26)$$

The horizontal momentum equations are forced analogously to the simulations by Klymak (2018) and Shakespeare et al. (2021a) to maintain a background zonal velocity $U(t) = U_{\text{mean}} + U_{\text{tidal}} \cos(\omega t)$. In particular, the x-momentum equation is forced with:

$$\frac{f^2 - \omega^2}{\omega} U_{\text{tidal}} \sin(\omega t), \qquad (27)$$

and the y-momentum equation with fU_{mean}.

Our general procedure was to run a test using reference values for N, h_0, W, H, f, ω, U_{mean} and U_{tidal}, before varying each parameter individually to determine their impact on the stress. For the purely tidal or steady flow tests, these default parameters are listed in Table 1. Note that the bottom-trapped tests are run at $90°S$ which, although unphysical, is fine in a simulation and allows us to study a regime whereby bottom-trapped effects truly dominate. For the mixed flow case, the parameters will either be the same as the tidal case with a mean velocity of $U_{\text{mean}} = 0.1$ m s^{-1} added, or the same as the mean case with a tidal velocity of $0.1 \cos(\omega t)$ m s^{-1} added. This will be made clear in the text. Also note that the default values of h_0 and H vary slightly between the two- and three-dimensional tests. This is due to it being more difficult to achieve high resolution for small hills in the three-dimensional case.

In each test, the main quantity we computed was the x-component of the stress, given as in (2) by:

$$F_{3\text{d}} = \frac{1}{\rho_0} \int\limits_{-L_y/2}^{L_y/2} \int\limits_{-L_x/2}^{L_x/2} p_h \frac{\partial h}{\partial x} \mathrm{d}x\mathrm{d}y, \qquad (28)$$

where $p_h(x, y)$ is the bottom pressure, i.e., the pressure values that corresponds to the grid cell directly above the hill at horizontal position (x, y).

The default values in columns 1 and 2 of Table 1 were chosen to be within the usual linear regimes. This allowed us to clearly see any non-linear effects that arose when the parameters are varied. For the tidal tests in column 1, a standard measure of non-linearity for propagating waves with $|f| < \omega$ is the steepness parameter, defined by (see e.g. Balmforth et al. (2002))

$$s = k h_0 \frac{\sqrt{N^2 - \alpha\omega^2}}{\sqrt{\omega^2 - f^2}}. \qquad (29)$$

For the default values in Table 1 with $|f| = 5 \times 10^{-5}$ and $\omega = 1.4 \times 10^{-4}$, setting k to be the dominant wavenumber ($k = 1/W$) gives $s \approx 0.6$ which is within the "subcritical" regime $s \lesssim 1$. Then, for the default steady tests in column 2 of Table 1, the Froude number is given by $Fr = 0.2$ for the two-dimensional tests, and $Fr = 0.3$ for the three-dimensional tests, both of which are well within the linear regime.

For efficiency, all simulations were run in hydrostatic mode, using the *HydrostaticFreeSurfaceModel* in Oceananigans. The unimportance of non-hydrostatic processes for the stress is reflected by the parametrisations in Section 2, whereby the hydrostatic ($\alpha = 0$) and non-hydrostatic ($\alpha = 1$) parametrisations are essentially the same provided the buoyancy frequency N is large compared to the wave frequency. More precisely, non-hydrostatic effects are deemed unimportant for $N \gg \omega$ for tidal flows, and $N \gg kU$ for mean flows, which holds for the parameters considered here. Each three-dimensional tidal test was run for 200 hours, whereas each three-dimensional steady test was run for 100 hours. We found that 100 hours was generally long enough to reach a near-equilibrium state, with the slightly longer test time given for tidal tests as to have more full tidal cycles to perform a statistical analysis on. Since two-dimensional tests were much less computationally expensive, we decided to run them for even longer (750 hours) to improve accuracy and detect any notable effects that only appeared at later times. We timestep all simulations using a 2nd-order quasi Adams-Bashforth time stepping scheme. The free surface was sub-stepped with the split-explicit free surface solver described by Shchepetkin and McWilliams (2005). All simulations used time-step of 7.5 minutes, and an output interval of 15 minutes.

4. Results and Evaluation

We now compare the parametrisations in Section 2 with the numerical data from the model described in Section 3. We consider results separately depending on the type of flow (tidal, steady or mixed) and the number of dimensions (two or three).

For each of the purely tidal flow simulations, we assume that (the x-component of) the stress is periodic and of the form

$$\text{Stress}(t) = A\cos(\Omega t + \phi), \tag{30}$$

for some determinable values of the amplitude A, frequency Ω and phase ϕ. To compute these values, we first extract the last 200 values (corresponding to 40 hours) of the stress output by the model, computed as per (1) or (28), depending on the dimension under consideration. We then fit these 200 values to a cosine curve. To calculate uncertainty, we recompute these values for the last 100 values and the last 101–200 values, recording the difference from the initially obtained values.

For each of the purely steady flow simulations, we use the average value of the stress over the last 20 hours of simulation. The uncertainty is then computed using the minimum and maximum values of the stress during these last 20 hours.

Finally, for the mixed flow simulations, we assume the stress is of the form (cf. (21))

$$\text{Stress}(t) = F_m + F_p\cos(\Omega t + \phi), \tag{31}$$

with both a mean component F_m and a periodic component $F_p\cos(\Omega t + \phi)$. To compute F_m and F_p we fit the last 200 output values of the stress to a shifted cosine curve of the form (31). The uncertainty in F_m and F_p is obtained by recomputing for the last 100 values and 101–200 values and recording any difference.

a. Tidal flow in two dimensions

We first consider tidal flow over an isolated hill in two dimensions. For each simulation, the computed stress is compared to the parametrisations in Section 2a. Figure 2 shows this comparison for the parametrisation F_{SAH2d} (see (11)) when the parameters U_{tidal}, N, f, W, H and h_0 are varied. Although not explicitly shown in Figure 2, the simpler JSL2001 parametrisation (Equation (3)) predicts the same scaling as F_{SAH2d} with respect to the stratification N, hill height h_0 and tidal speed U_{tidal}. Thus our analysis for these variables also holds true for the JSL2001 theory.

For most of the simulations, the flow is forced with the semi-diurnal M_2 constituent, with $\omega = 1.4 \times 10^{-4}$ s^{-1}. The only exception is for the bottom-trapped ($|f| > \omega$) tests displayed in Figure 2h, whereby we use the diurnal K_1 constituent ($\omega = 7.3 \times 10^{-5}$ s^{-1}). This is because on Earth, bottom-trapped effects are more common for diurnal constituents than semi-diurnal constituents. In particular,

for a diurnal constituent the frequency ω is smaller and thus $|f| > \omega$ for a larger range of latitudes. However, note that we also performed a small number of tests with $|f| > \omega$ for the M_2 tide. This appears as part of our tests varying f (Figure 2c), in the case when the latitude is greater than $75°$.

In general, the parametrisation F_{SAH2d} performs well compared to the simulations. However, in most cases the theoretical prediction slightly underestimates the stress. This is to be expected as the parametrisations from JSL2001 and SAH2020 are derived in an idealised regime whereby the topographic height and flow speed are assumed to be small. There are thus other non-linear effects that are not accounted for which could contribute to the drag. For instance, calculations of Balmforth et al. (2002) show that the energy flux should increase by around 14% above the linear theory for isolated Gaussian hills as the steepness parameter (defined in (29)) goes from 0 to 1, which we expect should also translate to form stress.

Looking at Figures 2a and 2b, we see that the predicted linear scaling by the tidal speed U_{tidal} and the buoyancy frequency N matches the simulations almost precisely. The same is true for the $\sqrt{\omega^2 - f^2}/\omega$ scaling for the Coriolis parameter f (Figure 2c), highlighting the importance of accounting for latitude in tidal stress, which is neglected in the JSL2001 parametrisation.

However, for the simulations varying the hill width W, ocean depth H and hill height h_0 (Figures 2d–2h), there are some larger discrepancies between the computed stress and F_{SAH2d}. Firstly for the tests varying W we see a small increase in the drag as W increases. Note that a priori we do expect some dependence of the stress on W despite it not appearing in F_{SAH2d}. This is because a wider hill gives more area for waves reflected off the surface to interact with topography, as discussed around (7). Additionally, we also note that the slope criticality (see (29)) directly depends on the wavenumber k and thus W.

Next, for the tests varying the ocean depth H and hill height h_0 (Figures 2e–g) we find that, provided $|f| < \omega$, the flow in the vicinity of the hill speeds up as it moves over the narrow channel at the top of the hill. As a result, one finds that F_{SAH2d} underestimates the stress particularly when h_0 is large or H is small. Thus, to better model the stress for the H and h_0 tests we also consider a refinement of the F_{SAH2d} parametrisation with a scaled velocity

$$U_m(t) = \frac{H}{H - h_0}U(t), \tag{32}$$

inspired by the steady flow parametrisation F_{KLP} (see (19)). Here, the factor of $H/(H - h_0)$ is the ratio of the ocean depth H away from the hill, to the ocean depth $H - h_0$ at the centre of the hill. For medium-sized hills replacing $U(t)$ with $U_m(t)$ in F_{SAH2d} more accurately matches our simulation data. However, we also find that

TABLE 1. The default parameter values used for the tests with a purely tidal or steady flow in either two dimensions (2d) or three dimensions (3d). Here N is the buoyancy frequency, h_0 is the hill height, W is the hill width, H is the ocean depth, f is the Coriolis parameter, ω is the tidal frequency, U_{mean} is the mean flow speed and U_{tidal} is the amplitude of the periodic component of the flow. For the tidal flow tests, the choice of ω and f (and thus latitude) will be made clear in the text. The parameters for the steady flow tests also vary depending on whether we are interested in a low or high Froude number $Fr = Nh_0/U_{\text{mean}}$ regime.

	Tidal	Steady ($Fr \lesssim 1$)	Steady ($Fr \gg 1$)
N (s^{-1})	4×10^{-3}	2×10^{-3}	5×10^{-3}
h_0 (m)	100	20 (2d) or 30 (3d)	500
W (m)	5000	5000	5000
H (m)	1500	1500 (2d) or 1250 (3d)	1500
f (s^{-1})	-5×10^{-5} or -1.46×10^{-4}	-2.53×10^{-5}	0
Latitude (°S)	20 or 90	10	0
ω (s^{-1})	1.4×10^{-4} or 7.3×10^{-5}	–	–
U_{mean} (m s^{-1})	0	0.2	0.1
$Fr = Nh_0/U_{\text{mean}}$	–	0.2 (2d) or 0.3 (3d)	25
U_{tidal} (m s^{-1})	0.1	0	0

the scaling $U_m(t)$ "saturates" around $h_0 \approx H/2$ in the sense that using the velocity scaling

$$\widetilde{U}_m(t) = \begin{cases} \dfrac{H}{H - h_0} U(t), & h_0 \leq H/2 \\ 2\,U(t), & h_0 > H/2 \end{cases} \quad (33)$$

yields better results for large values of h_0. In particular, for our tests varying h_0 in Figures 2f and 2g, we see that incorporating $\widetilde{U}_m(t)$ into the F_{SAH2d} parametrisation gives a stress profile that is much closer to the simulation data. The only exception is when the hill crest is close to the surface ($h_0 \approx H$) and the stress plateaus (Figure 2g). We remark that for our tests, there is a discontinuity in the derivative (with respect to h_0) of $\widetilde{U}_m(t)$ at $h_0 = 750$ m. However, this is not shown explicitly in Figure 2 since the discontinuity is at the point which separates Figures 2f and 2g. For our tests varying H, a similar improvement upon using $\widetilde{U}_m(t)$ can then be seen in Figure 2e. However, even with the $\widetilde{U}_m(t)$ scaling, F_{SAH2d} still underestimates the model output as H decreases. This is not unexpected as wave reflections become more important in this limit (see discussion around (7)).

We now consider the results for bottom-trapped flows with $|f| \geq \omega$ (Figure 2h), which were performed for the K1 tidal constituent at a latitude of 90°. For these tests, in contrast to the $|f| < \omega$ case, we found that the F_{SAH2d} parametrisation remains relatively accurate as h_0 increases (Figure 2h). This is expected as such flows have a different velocity profile compared to the $|f| < \omega$ case. Namely, when $|f| \geq \omega$, the flow still speeds up at the top of the hill but is slowed down or "trapped" at the base of the hill. Thus

in this case, it is not accurate to use the $\widetilde{U}_m$ scaling, which assumes the current speeds up along the entire length of the hill.

Finally, as defined in (30), it remains to analyse the frequency Ω and phase ϕ of the simulated stress and how it compares to the parametrisations. Here, we first remark that the fitted frequency from our simulation data closely matches the tidal frequency: in each case the two quantities are within 1% of each other. However, the phase data is more interesting and for the tests varying f, this is shown in Figure 3. Here, the F_{SAH2d} parametrisation suggests that in the absence of wave reflections, the stress should be in phase with $U(t)$ when $|f| < \omega$ and then 90° (or 1/4 of a tidal period) out of phase with $U(t)$ when $|f| > \omega$. Note that we give the phase in hours, obtained by multiplying ϕ by $\omega/2\pi$. Most of our simulations accurately reflect this prediction, yielding a phase within half an hour of that predicted by F_{SAH2d}. The only exception is when the latitude is very close to the critical value where $|f| = \omega = 1.4 \times 10^{-4}s$ or approximately $74.5°S$. In this exceptional case, the phase is near the half-way point between the predicted subcritical ($|f| < \omega$) and supercritical ($|f| > \omega$) phase. This behaviour is exactly what one would expect from Fourier analysis. However, there would be little practical value in adding this exceptional case to the F_{SAH2d} parametrisation. Ultimately though, our results for the phase further support including an f dependency in stress parametrisations, which is not present in the JSL2001 parametrisation.
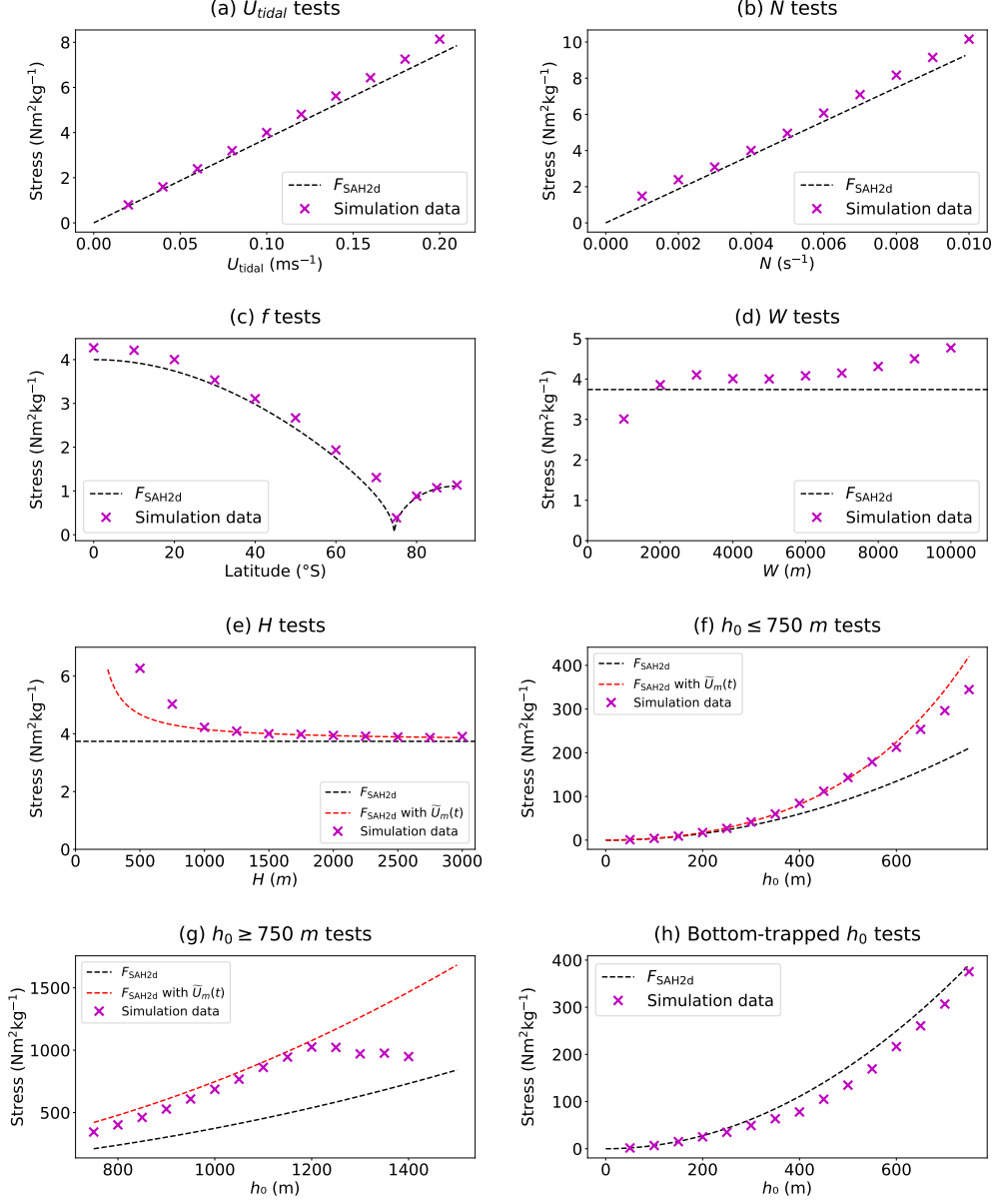
FIG. 2. The amplitude of the oscillatory stress given by F_{SAH2d} and the simulation data for two-dimensional tidal flow. In Figures (e)–(g) a refinement of the F_{SAH2d} parametrisation with a scaled velocity (see Equation (33)) is also shown in red. The default parameters for each test are as in Table 1 with $\omega = 10^{-4}$ s^{-1} (M_2 tide) at a latitude of $20°S$ ($f = 5 \times 10^{-5}$ s^{-1}). The only exception is the bottom-trapped tests in Figure (h) which use $\omega = 7.3 \times 10^{-5}$ s^{-1} (K_1 tide) at a latitude of $90°S$ ($f = 1.46 \times 10^{-4}$ s^{-1}). In all tests, the uncertainty in the computed stress was less than 3% so the small error bars have been omitted.

b. Tidal flow in three dimensions

Our results for tidal flow in three dimensions are analysed analogously to our results in two dimensions. Note that in what follows, we compute the x-component of the stress amplitude, frequency and phase. Figure 4 shows a comparison between F_{SAH3d} (Equation (10)) and the simulation data as the tidal speed U_{tidal}, hill width W, Coriolis parameter f and hill height h_0 are varied. Plots of the phase are also included for tests that vary the latitude (or equivalently f).

Similar to the two-dimensional case, the simulations varying U_{tidal}, W and f (Figures 4a–4c) qualitatively reflect the scaling predicted by the F_{SAH3d} parametrisation.

For the tests varying f, the F_{SAH3d} parametrisation well approximates the model output for near-zero $|f|$. However, there is an almost linearly increasing error as f increases. As this effect did not occur in two-dimensions, there must
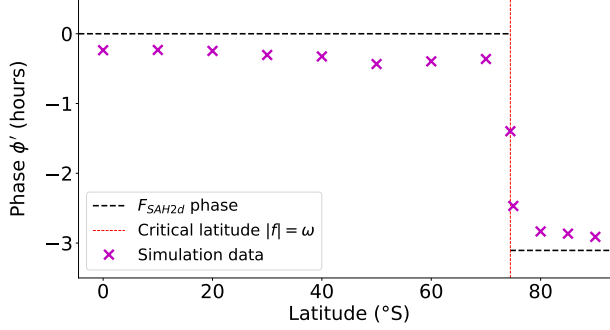
FⁱG. 3. The fitted phase of the stress for our two-dimensional tidal flow simulations varying latitude. Here, the phase $\phi' = \phi \times (\omega/2\pi)$ is given in hours as opposed to radians (cf. (30)), and the critical latitude ($\approx 74.5°S$) is displayed in red. In each test, the uncertainty was less than 0.05 hours so the small error bars have been omitted.

be something specific to three-dimensions causing this discrepancy. As $|f|$ increases, there is increasing flow in the y direction which in three-dimensions (unlike two) is permitted to vary in y, and we speculate that this additional degree of freedom is likely responsible for the growing error, although the details remain uncertain.

We now consider tests varying h_0. In the bottom-trapped ($|f| > \omega$) case, the simulated data matches the scaling predicted by the F_{SAH3d} parametrisation (Figure 4d). However, for our choice of parameters, F_{SAH3d} overestimates the simulated stress by more than in the two-dimensional case. In particular, over all the tests we performed, F_{SAH3d} was on average 46% larger than the simulated stress in three-dimensions, compared to 18% for F_{SAH2d} in two-dimensions. In the case where $|f| < \omega$ there is then a qualitative difference between the computed stress profile and that predicted by F_{SAH3d}, depending on whether the hill width W is small or large (Figures 4e and 4f). To account for this difference, we let $\widetilde{F}_{SAH3d}$ be equal to F_{SAH3d} but with the velocity scaling $\widetilde{U}_m$ (Equation (33)) discussed in the two-dimensional setting. For large W (Figure 4f), the scaling of the stress is the same as in the two-dimensional case. Namely, $\widetilde{F}_{SAH3d}$ matches the stress profile until $h_0 \approx H$. However, for our default width $W = 5000\ m$, $\widetilde{F}_{SAH3d}$ only matches the simulated stress for small–medium values of h_0 (Figure 4e). Then, for $h_0 \gtrsim 500\ m$, the stress is much closer to the unscaled F_{SAH3d} parametrisation. Since $\widetilde{F}_{SAH3d}$ is only slightly larger than F_{SAH3d} for small hill heights, it thus seems reasonable to just apply the unscaled parametrisation F_{SAH3d} for all values of h_0 in this "small W" regime. We remark that this regime shift for smaller W is not entirely unexpected, as provided W is not too large, we expect some of the current to flow around the hill, rather than be forced over the top as in the two-dimensional case. Future work should identify more precisely at what values of W this regime shift occurs.

Finally, we remark that, as with the two-dimensional case, the frequency and phase accurately matches the values predicted by the SAH2020 theory. However, the most notable difference in three dimensions is a smoother transition from the stress being in phase when $|f| < \omega$ to being 90° out of phase when $|f| > \omega$ (Figure 4h). Nevertheless, this effect was only clear when $|f|$ was very close to ω so that the phase predicted in F_{SAH3d} is still accurate for almost all values of f.

c. Steady flow in two dimensions

For two-dimensional tests with a steady flow we compare the computed stress (denoted F_{2d}) with the parametrisations F_{Bell2d} and F_{KLP} from Section 2. In particular, tests with low Froude numbers $Fr \lesssim 1$ are compared with F_{Bell2d} and tests with high Froude numbers $Fr \gg 1$ are compared with F_{KLP}.

Figure 5a shows our comparison between the simulated data and F_{Bell2d} for Froude numbers in the range $0.1 - 1$. We see that although the scaling used in Bell's theory is generally accurate, F_{Bell2d} typically underestimates the stress by about 50%, and even more so as the Froude number approaches 1. Hence, Bell's parametrisation should ideally be adjusted to depend on Fr. In this regard, one could define a scaled parametrisation

$$\widetilde{F}_{Bell2d} = \frac{1}{A_1 - B_1(Nh_0/U)} F_{Bell2d}, \qquad (34)$$

for constants A_1, B_1, and $Fr \lesssim 1$. Note that the linear trend line in Figure 5a corresponds to the values $A_1 = 0.71$ and $B_1 = 0.46$. However, a parametrisation of the form (34) still does not describe the full behaviour of the stress in the regime $Fr \lesssim 1$. Namely, in Figure 5b we also see a non-linear relationship between the stress and latitude. This reinforces that, even for low Froude numbers, non-wave and non-linear effects manifest that are not accounted for by Bell's theory. We also remark that the trend line in Figure 5a is the opposite to what one gets with energy flux calculations. That is, as the Froude number increases, one reaches a saturation of lee waves and Bell's formula for energy flux becomes an overestimate (see (17)).
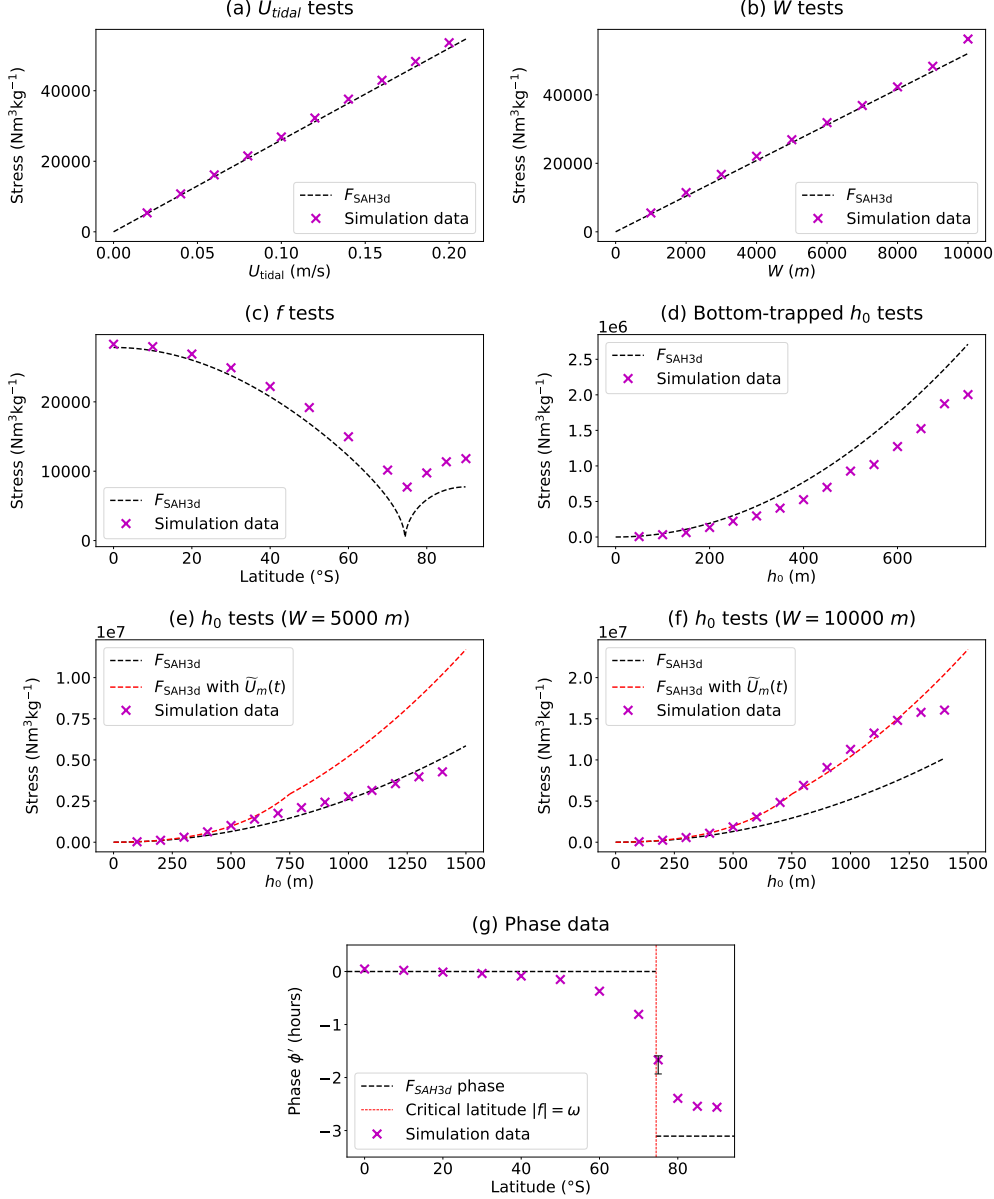
FIG. 4. The amplitude of the oscillatory stress given by F_{SAH3d} and the simulation data for three-dimensional tidal flow (panels (a)–(f)), and the phase of the stress as the latitude is varied (panel (g)). The default values for each test are the same as the two-dimensional case (see Figure 2 and Table 1). In panels (a)–(f), the uncertainty in the computed values was less than 10% so the small error bars have been omitted. In Figure (g), error bars have only been included in the single case where the uncertainty in the phase was greater than 0.1 hours.

Figures 5c–5e then show our comparison between the simulated data and F_{KLP} for large Froude numbers and $f = 0$. Here, the approximately linear scaling of buoyancy frequency N and flow speed U in F_{KLP} seems to be very accurate (Figures 5c and 5d). On the other hand, the height scaling of $h_0^2 H/(H - h_0)$ overestimates the stress as the hill height h_0 gets large (Figure 5e). Our results indicate that a simpler scaling than that in F_{KLP} is more accurate. In

particular, if we parametrise the stress as

$$\text{Stress} = C_1 N h_0^2 U, \qquad (35)$$

for some suitable constant C, then we get much closer to the drag from the simulations. For $C_1 = 1.4$ this is shown in Figure 5e. Moreover, using (35) as opposed to F_{KLP} gives a valid result for lower Froude numbers when F_{KLP} is negative (and thus unphysical).
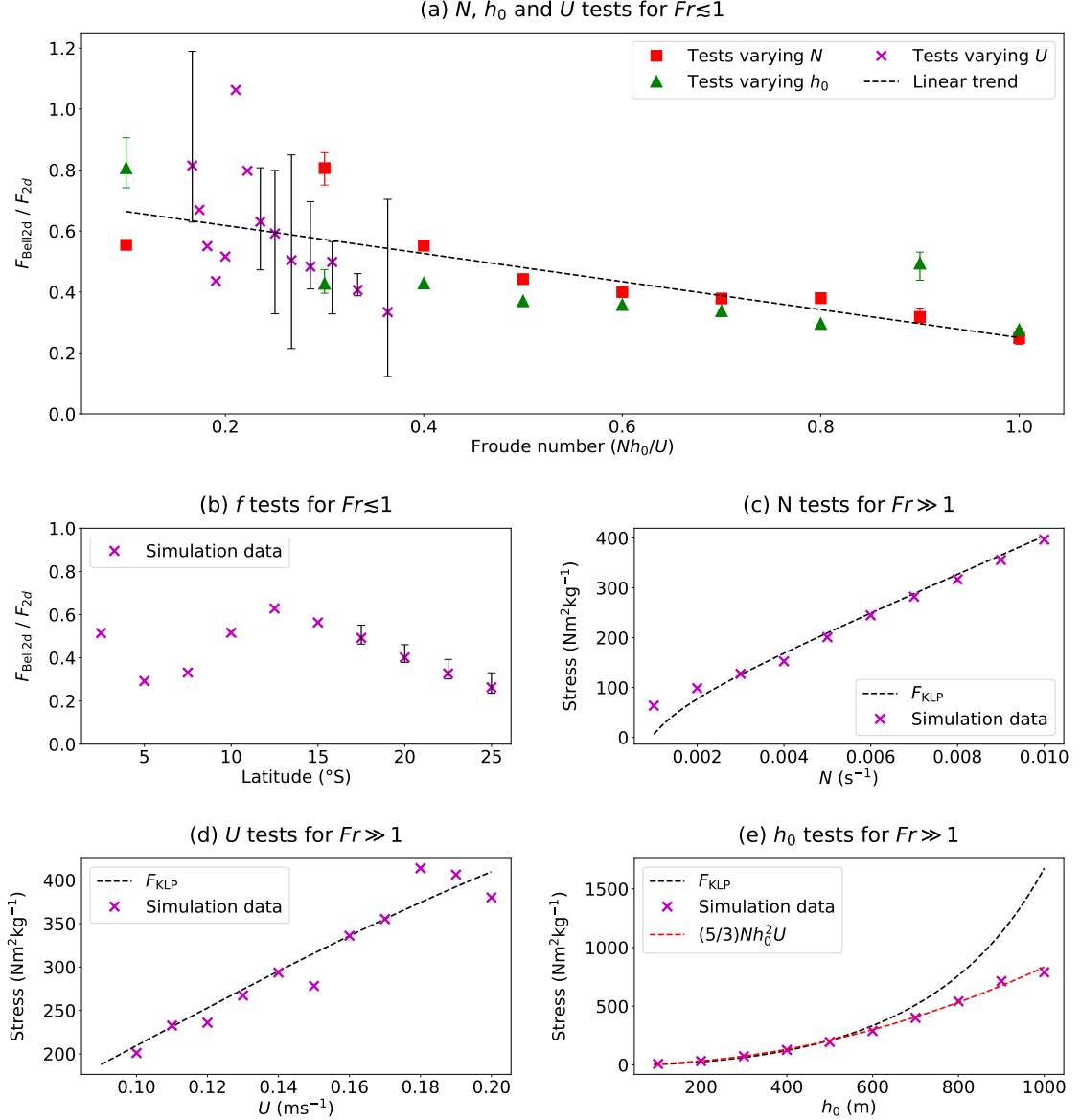
FIG. 5. A comparison of the stress predicted by the Bell (1975) and KLP2010 parametrisations with our simulation data for two-dimensional steady flow. Here, N denotes the buoyancy frequency, h_0 the hill height, U the flow speed, and f the Coriolis parameter. Note that for Figures (a) and (b), the ratio between the stress as predicted the Bell (1975) theory, F_{Bell2d}, and the stress output from the simulations, F_{2d}, is plotted. On the other hand, in Figures (c) to (e) the numerical values of the stress predicted by KLP2010 parametrisation, F_{KLP}, is shown. The default parameters are as in Table 1 and error bars are shown whenever the uncertainty in the stress was greater than 10%.

We also ran a few tests with rotation added to the high Froude number simulations. In this case, the stress was unstable and increased by several fold. Upon analysing the simulation data, we found that for these cases significant mixing occurred downslope, and gradually reduced the downstream stratification to zero. This phenomena is reminiscent of atmospheric downslope windstorms, which can occur near large-scale topography on land (see e.g., Peltier and Clark 1979; Scinocca and McFarlane 2000).

However, this effect was far less dramatic in our three-dimensional simulations, where the presence of a lateral flow helps to stabilise the stratification. Such effects are thus likely to be rare in practice, mostly restricted to ridge-like structures. Rather than attempting to parametrise this non-linear phenomena here, we instead refer the reader to the recent work of Zemskova and Grisouard (2022). Here, the energetics of a steady rotating flow over tall topography

is analysed in detail, and used to help explain observations in the Southern Ocean by Cusack et al. (2020).

d. Steady flow in three dimensions

For steady flow tests in three-dimensions, we again compare simulations with low Froude numbers $Fr \lesssim 1$ to the Bell (1975) theory. However, for tests with high Froude numbers $Fr \gg 1$, it does not make sense to compare our results directly to KLP2010 as this theory was only derived in the two-dimensional case. Thus, for high Froude numbers, we instead focus on how the stress scales with different parameters.

Figure 6 shows a comparison between the stress from our simulations (denoted F_{3d}) and F_{Bell3d} when the parameters h_0, N, U, f and W are varied. For tests varying the hill height h_0 and buoyancy frequency N (Figure 6a) we find, similar to the two-dimensional case, that F_{Bell3d} underestimates the stress but still gives a mostly accurate scaling (i.e. Stress $\propto Nh_0^2$). However, for tests that vary the flow speed U, Coriolis parameter f and hill width W (Figure 6b), we see that F_{Bell3d} significantly underestimates the stress as the Rossby number

$$Ro \stackrel{\text{def}}{=} \frac{U}{|f|W}, \tag{36}$$

decreases. In this regard, it is worth noting that via a change of variables, F_{Bell3d} can be expressed as

$$F_{\text{Bell3d}}\left(\alpha = 0, \ h(x,y) = h_0 e^{-(x^2+y^2)/2W^2}\right) =$$
$$= \text{Re}\left(\int_0^{2\pi}\int_0^\infty \tilde{K}e^{-\tilde{K}^2}\cos^2\theta\sqrt{\tilde{K}^2 - \frac{1}{Ro^2\cos^2\theta}}\,\mathrm{d}\tilde{K}\mathrm{d}\theta\right)Nh_0^2W\rho_0 \tag{37}$$

where $\tilde{K} = W\sqrt{k^2+\ell^2}$ and $(kW, \ell W) = (\tilde{K}\cos\theta, \tilde{K}\sin\theta)$. From (37) we see that as Ro increases so too does the lee wave stress. Therefore, a possible explanation for the discrepancy between F_{Bell3d} and the simulation data is that as Ro decreases, fewer lee waves are formed and the stress is instead generated by other non-linear motions such as partial blocking (see e.g., Trossman et al. 2016; Klymak et al. 2021). To parametrise this phenomenon, we note that from Figure 6b the ratio F_{Bell3d}/F_{3d} has a clear linear dependence on the ratio $|f|W/U$. In particular, our data points give a correlation coefficient between F_{Bell3d}/F_{3d} and $|f|W/U$ of $R^2 = 0.89$. This suggests that we should use the scaling

$$\widetilde{F}_{\text{Bell3d}} = \frac{1}{A_2 - B_2|fW/U|}F_{\text{Bell3d}} \tag{38}$$

for some constants A_2 and B_2 and $Fr \lesssim 1$. The linear trend line in 6b corresponds to $A_2 = 1.34$ and $B_2 = 0.88$.

Certainly, (38) should only be applied for small values of $|fW/U|$ so that the denominator $A_2 - B_2|fW/U|$ remains positive.

Figure 7 shows the results of our tests for the high Froude number $Fr \gg 1$ regime. In this case, we find that the stress deviates significantly from the approximate Nh_0^2WU scaling found in other regimes. Instead we find that the stress obeys a quadratic law, being proportional to h_0WU^2, similar to what one expects in the atmosphere (e.g., Lott and Miller 1997). In fact, the simple parametrisation, which sets the stress equal to h_0WU^2 (with proportionality constant 1) works remarkably well for our choice of parameters. However, as is usual with quadratic drag laws, it is likely that a different proportionality constant would be required if the shape of the topography differed substantially from a Gaussian hill. The stress then appears to be mostly independent of N and f (Figures 7d and 7e); only increasing or decreasing by small amounts as these parameters are varied. We note however, that for larger values of f, our computed value of the stress has a large uncertainty. These results can be directly compared to recent work of Klymak et al. (2021) which involved a similar analysis but with many, randomly distributed obstacles. Klymak et al. also observed this f independence for the stress but an approximately linear dependence on N for high Froude numbers. Therefore, we do not expect the stress to remain independent of N for more complicated non-isolated topography.

e. Mixed flow in two dimensions

We now analyse our results for mixed flows with a horizontal velocity of the form (20) and stress of the form (31). In what follows we let $\widetilde{F}_m$ and $\widetilde{F}_p$ be the values for F_m and F_p if U_{tidal} or U_{mean} are set to be zero respectively. In Figure 8 we show our computed values of $F_m/\widetilde{F}_m$ and $F_p/\widetilde{F}_p$ for a range of parameters. This lets us discern the impact of a tidal flow on a steady flow and vice versa. When the Froude number is small ($Fr \lesssim 1$) these ratios are also compared to the expected ratio from Bell's parametrisations defined in Sections 2b and 2c (Figures 8e and 8f).

To compute the uncertainty in our values of $F_m/\widetilde{F}_m$ and $F_p/\widetilde{F}_p$, we define F_m^-, $\widetilde{F}_m^-$, F_p^-, $\widetilde{F}_p^-$ and F_m^+, $\widetilde{F}_m^+$, F_p^+, $\widetilde{F}_p^+$ to respectively be the lower and upper values of uncertainty for each quantity. The lower and upper uncertainties in $F_m/\widetilde{F}_m$ and $F_p/\widetilde{F}_p$ are then given by

$$\left(\frac{F_m}{\widetilde{F}_m}\right)^\pm = \frac{F_m^\pm}{\widetilde{F}_m^\mp} \qquad \text{and} \qquad \left(\frac{F_p}{\widetilde{F}_p}\right)^\pm = \frac{F_p^\pm}{\widetilde{F}_p^\mp}. \tag{39}$$

First we consider our results for the mean component of the stress F_m. In general, for both low and high Froude numbers, we find that $F_m/\widetilde{F}_m \approx 1$, suggesting that the naive parametrisation $F_m = \widetilde{F}_m$ is accurate for a wide range of parameters. However, in some regimes we find that F_m
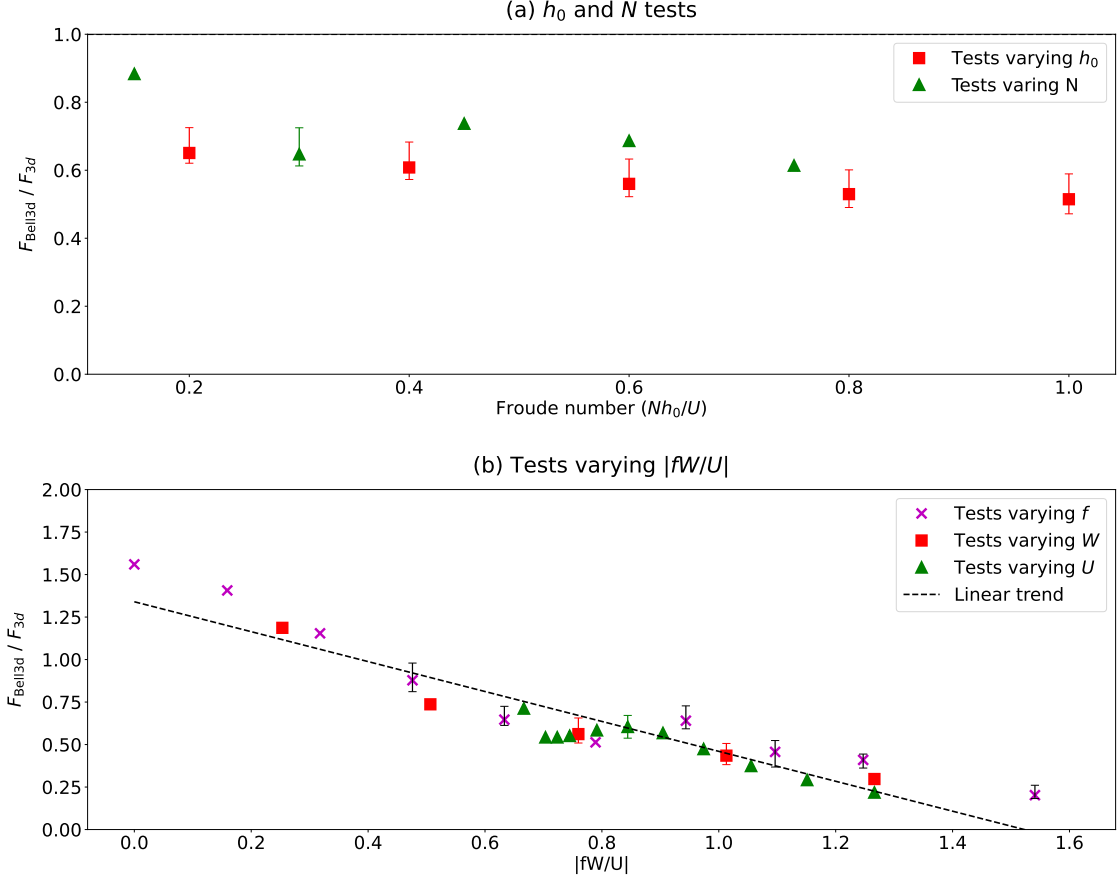
FIG. 6. A comparison of the stress predicted by the Bell (1975) parametrisation (F_{Bell3d}) and the simulation drag (F_{3d}) for three-dimensional steady flows with low Froude number ($Fr \lesssim 1$). The default parameters are as in Table 1 and error bars are shown whenever the uncertainty in the computed stress is greater than 10%.

notably exceeds $\widetilde{F}_m$. This is most evident in Figure 8e, where F_m can be over two times larger than $\widetilde{F}_m$ for small values of U_{mean}. This is reflected by Bell's formula (23), whereby as $U_{\text{mean}} \to 0$ we have $\omega_0 \to 0$ so that the $n = 0$ term becomes small and the $n \geq 1$ terms associated with the tide become more dominant. However, we note that using Bell's parametrisation, F_m exceeds $\widetilde{F}_m$ by more than what is reflected by the simulation data.

Our simulations also indicate that Bell's parametrisation is very inaccurate for larger Froude numbers $Fr \geq 1$, so that this parametrisation should not be extended to such a case. For instance, for our h_0 tests in Figure 8c we have $2 \leq Fr \leq 26$ and $F_m/\widetilde{F}_m \approx 1$. However, Bell's parametrisation gives the substantially larger value $F_m/\widetilde{F}_m = 21.38$.

Next we consider our results for the periodic component of the stress F_p. Similar to the mean component, we find in most regimes that $F_p/\widetilde{F}_p \approx 1$, thereby further highlighting the accuracy of the naive parametrisation $F_p = \widetilde{F}_p$. The most notable exception is near critical latitudes when $|f| \approx \omega$ (Figure 8b). This is to be expected as the steady

component of the flow acts to Doppler shift the tidal frequency ω. Therefore when $|f| = \omega$, we expect F_p to not approach zero unlike $\widetilde{F}_p$ (see (11)), leading to a large value of the ratio $F_p/\widetilde{F}_p$.

For low Froude numbers (Figures 8e and 8f) we also observe a dependence of $F_p/\widetilde{F}_p$ on the mean flow speed U_{mean} and the hill width W. In particular, $F_p/\widetilde{F}_p$ slightly exceeds 1 as U_{mean} increases (Figure 8e), and significantly exceeds 1 for small W (Figure 8f). This is likely linked to the fact that the classical lee wave frequency kU_{mean} depends explicitly on U_{mean} and implicitly on W. In particular, with the Fourier convention in (6), the wavenumber spectrum for a Gaussian hill $h(x) = h_0 e^{-x^2/(2W^2)}$ is

$$\hat{h}(k) = h_0 W \sqrt{2\pi} e^{-k^2 W^2/2}. \tag{40}$$

In terms of developing a refined parametrisation, one could fit a linear trend line for $F_p/\widetilde{F}_p$ against U_{mean}. However, we are not sure how useful this would be since the increase in $F_p/\widetilde{F}_p$ is only small with U_{mean} and it is clear that W is
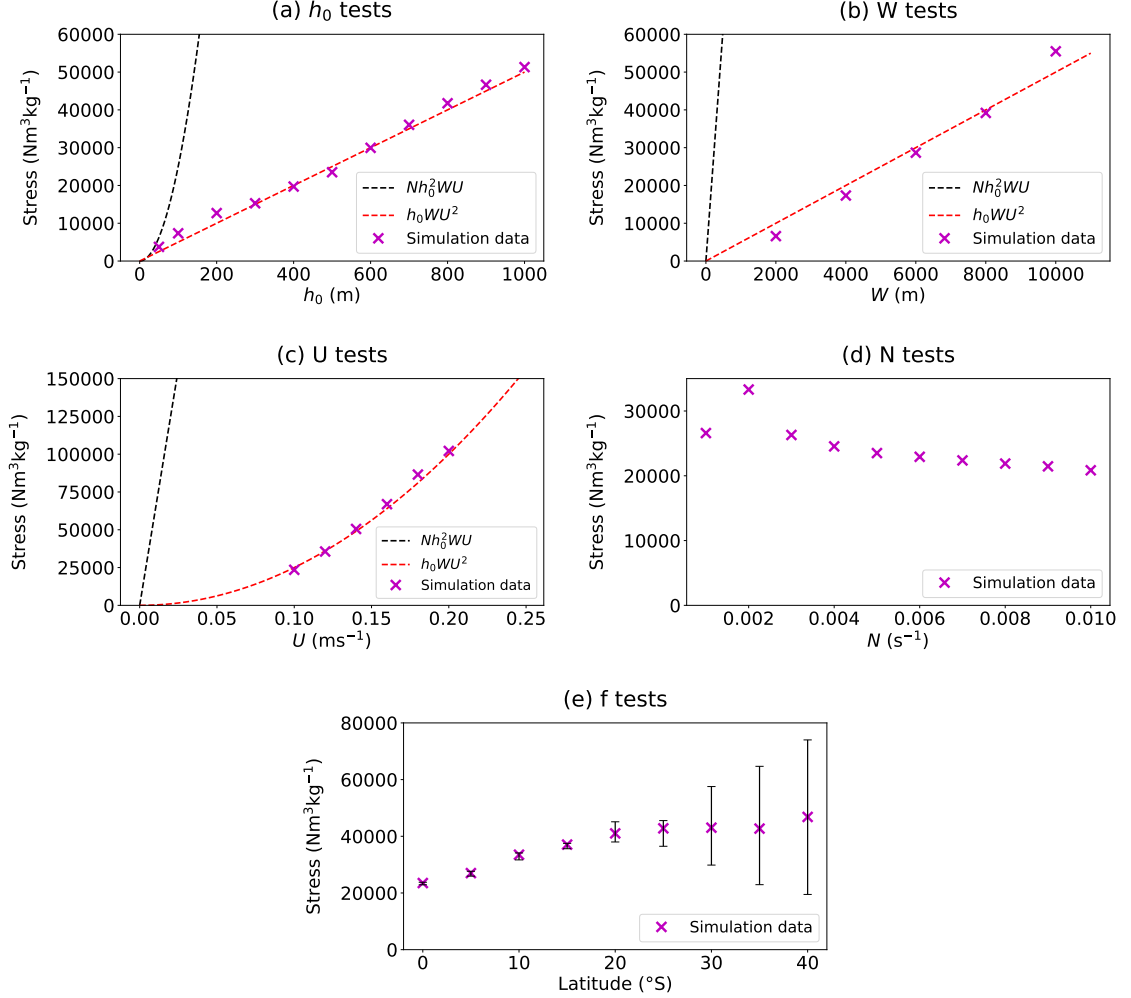
Fig. 7. Topographic stress for three-dimensional steady flows with high Froude number ($Fr \gg 1$). In panels (a)–(c), the drag from the simulation data is compared with both a linear $Nh_0^2 WU$ and quadratic $h_0 WU^2$ scaling. The default parameters are as in Table 1. Note that in panels (a)–(d) the uncertainty in the computed stress was always less than 10% so the small error bars have been omitted.

the far more sensitive parameter. It appears difficult however, to develop a more accurate parametrisation for small W, especially given how non-linear the trend is between $F_p/\widetilde{F_p}$ and W in Figure 8f. Notably, low values of W correspond to large values of the steepness parameter (see (29)), so that non-linear effects are expected to take place in this regime.

We also investigate the change in phase from a purely tidal flow to a mixed flow. In what follows we set ϕ_{tidal} and ϕ_{mixed} to be the respective phases for a purely tidal and a mixed flow with the same choice of parameters (besides the presence of a mean flow $U_{\text{mean}} = 0.1$ m s^{-1} in the mixed case). When $|f| \ll \omega$, we find that both ϕ_{tidal} and ϕ_{mixed} are approximately in phase with the velocity $U(t)$. However, as f increases, ϕ_{tidal} increasingly deviates from ϕ_{mixed}. In Figure 8g this is shown for our tests varying latitude (cf. Figure 8b), whereby the difference between ϕ_{tidal} and

ϕ_{mixed} reaches about 5 hours at $80°S$. This effect was also observed in a small number of supplementary simulations (not shown) for other tidal constituents besides M_2.

f. Mixed flow in three dimensions

Finally we consider mixed flows in three dimensions, with our results for this regime shown in Figure 9. Note that we use the same notation as in Section 4e. Like the two-dimensional case, we also find that $F_m/\widetilde{F_m} \approx 1$ and $F_p/\widetilde{F_p} \approx 1$ for the majority of tests. In fact, this approximation appears to hold true even more than in the two-dimensional case (cf. Figure 8).

Of particular note is the far less dramatic increase in $F_p/\widetilde{F_p}$ near the critical latitude $|f| \approx \omega$. This behaviour seems primarily related to our previous observations for
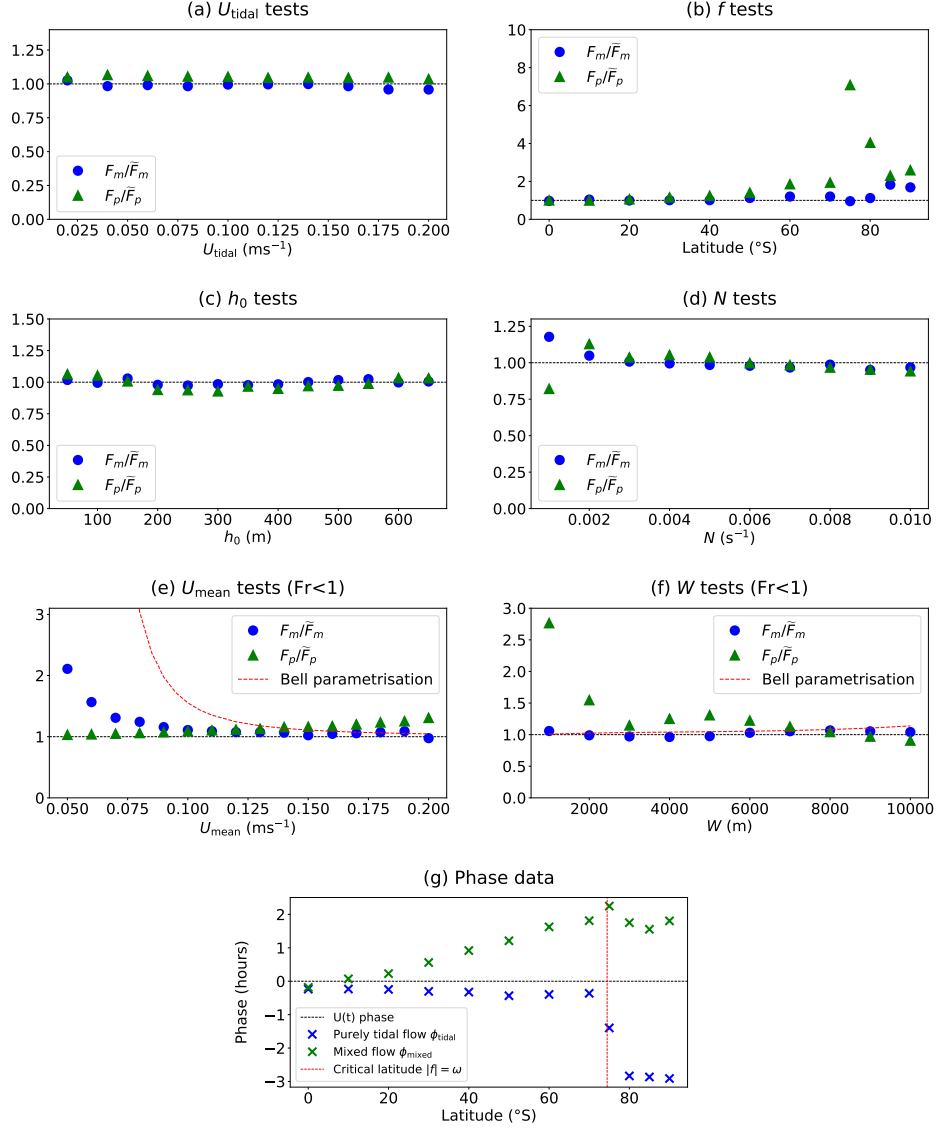
FIG. 8. Results for two-dimensional mixed flow simulations. In panels (a)–(d), the value of the ratios $F_m/\widetilde{F}_m$ and $F_p/\widetilde{F}_p$ are shown using $U_{\text{mean}} = 0.1 \text{ ms}^{-1}$ and the default parameters from our tidal tests (Figure 2). In panels (e) and (f), our results for low Froude numbers are displayed using $U_{\text{tidal}} = 0.1 \text{ ms}^{-1}$, an M_2 tidal frequency, and the default parameters from our steady flow tests (Figure 5). In Figure (g), our results for the phase shift for both the tidal ($\widetilde{F}_p$) and mixed (F_p) cases are shown for the simulations that varied latitude (cf. Figure (b)). In each test, the uncertainty was always less than 10% (or less than 0.2 hours for Figure (g)) so the small error bars have been omitted.

purely tidal flows, rather than some new phenomena specifically linked to three-dimensional mixed flows. Namely, in two-dimensions $\widetilde{F}_p$ essentially reaches 0 at the critical latitude (Figure 2c) causing the periodic component of the mixed (and thus Doppler-shifted) stress F_p to be very large by comparison. Then, by contrast, in three dimensions the value of $\widetilde{F}_p$ does not approach zero when $|f| = \omega$ (Figure 4c), resulting in a more subdued peak for the ratio $F_p/\widetilde{F}_p$.

Another notable observation in Figure 9 is the distinct increase in the ratio $F_m/\widetilde{F}_m$ as h_0 increases (Figure 9c),

which was not observed in the two-dimensional setting. To try to understand this increase, we recall the results from our purely steady flow tests with large Froude number in three dimensions (see Figure 7). For this regime, the mean stress followed a quadratic drag law, being proportional to $h_0 W U^2$ as opposed to the $h_0^2 W U$ scaling for low Froude numbers. Thus, averaging over one tidal period T, one

expects that for large Froude numbers

$$\frac{F_m}{\widetilde{F_m}} = \frac{1}{h_0 W U_{\text{mean}}^2 T} \int_0^T h_0 W \left[U_{\text{mean}} + U_{\text{tidal}} \cos(\omega t)\right]^2 \mathrm{d}t \tag{41}$$

$$= 1 + \frac{U_{\text{tidal}}^2}{2 U_{\text{mean}}^2}. \tag{42}$$

For the case $U_{\text{tidal}} = U_{\text{mean}} = 0.1$ represented in Figure 9c, this gives $F_m/\widetilde{F_m} = 1.5$, which is not too far off the model output for the larger values of h_0. In future work, it would be useful to understand this phenomenon further. In particular, it would be worthwhile evaluating the formula (42) throughout a wider parameter space. Moreover, it would also be useful to better understand the location and behavior of the transition between the low and high Froude number regime. Based on the limited data in Figure 4 this transition appears around $Fr \approx 10 - 20$, and corresponds to larger uncertainty in $F_m/\widetilde{F_m}$.

The other key difference in the three-dimensional setting is the value of the phase for mixed flows. In Figure 9g we see that the mixed flow phase is close to 0 so that the total stress is given by

$$F_{3d} = F_m + F_p \cos(\omega t + \phi), \tag{43}$$

with $\phi \approx 0$. By comparison, in two dimensions we found that ϕ was much larger as $|f|$ increased (Figure 8g). Such an effect is also in contrast to the purely tidal flow case, whereby the phase ϕ approaches $-\pi/2$ for large $|f|$.

5. Discussion and summary of suggested parametrisations

In the previous section, we tested existing topographic stress parametrisations for oceanic flows against a suite of simulations. Particular parametrisations of interest were those of Jayne and St. Laurent (2001) and Shakespeare et al. (2020) for tidal flows, as well as Bell (1975) and Klymak et al. (2010) for steady flows. Spanning a wide parameter space for an isolated Gaussian hill, we found that in many cases these parametrisations proved accurate, in many cases even when tested beyond the validity of their underlying assumptions. However, there were also regimes in which these existing parametrisations fell short, suggesting the need for an alternate or modified parametrisation.

We also studied the case of a mixed flow in Sections 4e and 4f. Here, we primarily compared our simulation data against the naive parametrisation which assumes that the tidal and steady components of a flow are independent. Our data yielded the cases for which this naive parametrisation was accurate, and cases for which a more sophisticated parametrisation needs to be developed.

In what follows, we summarise our suggested parametrisations based on our results in Section 4. Here, as in Section 2, F_{2d} and F_{3d} denote the stress in two and three dimensions respectively.

a. Suggested tidal flow parametrisations

For a purely tidal flow, we found that the parametrisations F_{SAH2d} (Equation (11)) and F_{SAH3d} (Equation (10)) due to Shakespeare et al. (2020, 2021a) were very accurate, mainly just requiring a small modification for large hill heights. In particular, for a purely oscillatory (tidal) flow in two dimensions, we suggest setting

$$F_{2d} = \frac{H}{H - h_0} F_{\text{SAH2d}}, \qquad \text{if } h_0 \leq H/2,$$
$$F_{2d} = 2 F_{\text{SAH2d}}, \qquad \text{if } h_0 > H/2,$$

noting that this parametrisation may overestimate the stress when $h_0 \to H$.

In three dimensions, we then similarly suggest setting

$$F_{3d} = \frac{H}{H - h_0} F_{\text{SAH3d}}, \qquad \text{if } h_0 \leq H/2,$$
$$F_{3d} = 2 F_{\text{SAH3d}}, \qquad \text{if } h_0 > H/2,$$

for large hill widths W, where F_{SAH3d} is as in (10). From our testing, $W = 10000$ m was a sufficiently large width to notice this effect (with $h_0 = 100$ m). For more modest values of W, we instead suggest setting $F_{3d} = F_{\text{SAH3d}}$.

b. Suggested steady flow parametrisations

For a purely steady flow, we found that the parametrisations due to Bell (1975) and Klymak et al. (2010) had mostly accurate scalings. However, to better match the simulation data we suggest introducing additional parameters that account for non-linear effects and need to be suitably chosen.

For a purely steady flow in two dimensions, we suggest setting

$$F_{2d} = \frac{1}{A_1 - B_1 Fr} F_{\text{Bell2d}}, \qquad \text{if } Fr \lesssim 1, \tag{44}$$
$$F_{2d} = C_1 N h_0^2 U, \qquad \text{if } Fr \gg 1, \tag{45}$$

where A_1, B_1 and C_1 are tunable constants, $Fr = N h_0/U$, and F_{Bell2d} is as defined in (14). Our data gave the fitted values $A_1 = 0.71$, $B_1 = 0.46$ and $C_1 = 1.4$. Note that one can use the Taylor expansion of (44) for small Froude numbers ($Fr \ll 1$) to obtain an expression with polynomial dependence on Fr. The extreme cases of low and high Froude numbers covers many possible regimes in the real world, for example abyssal hills for low Fr and seamounts for large Fr. However, we did not analyse the transitional case of medium Froude numbers ($Fr \approx 1 - 10$) in detail. For this, we refer the reader to the recent work of Klymak
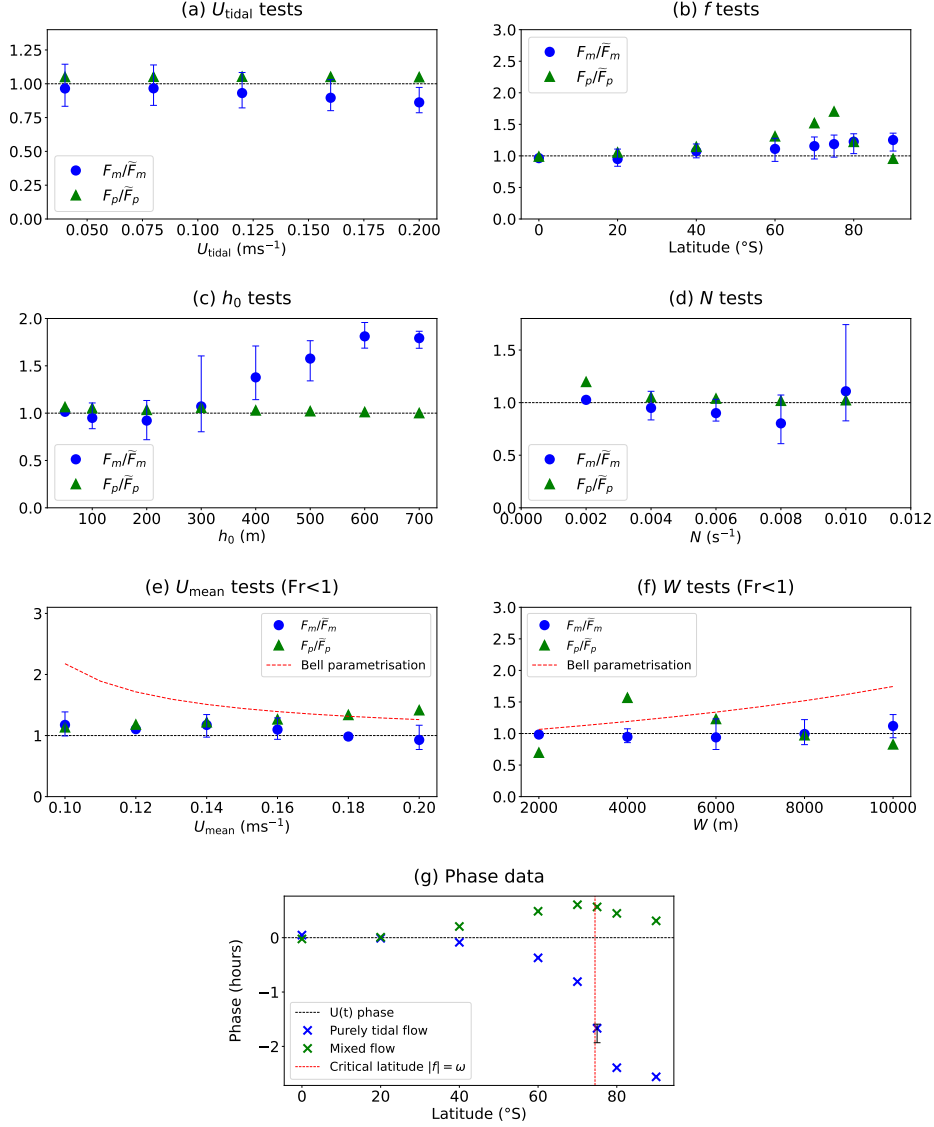
FIG. 9. Results for three-dimensional mixed flow simulations. In panels (a)–(d), the value of the ratios $F_m/\widetilde{F}_m$ and $F_p/\widetilde{F}_p$ are shown using $U_{\text{mean}} = 0.1 \text{ ms}^{-1}$ and the default parameters from our tidal tests (Figure 4). In panels (e) and (f), our results for low Froude numbers are displayed using $U_{\text{tidal}} = 0.1 \text{ ms}^{-1}$, an M_2 tidal frequency, and the default parameters from our steady flow tests (Figure 6). In Figure (g), our results for the phase shift for both the tidal ($\widetilde{F}_P$) and mixed (F_P) cases are shown for the simulations that varied latitude (cf. Figure (b)). In panels (a)–(f), error bars are only shown when the uncertainty is greater than 10%. In Figure (g), error bars are only displayed in the single case where the uncertainty was greater than 0.2 hours.

et al. (2021) where a hybrid parametrisation is tested to account for this additional regime.

In three-dimensions, we then suggest setting

$$F_{\text{3d}} = \frac{1}{A_2 - B_2|fW/U|}F_{\text{Bell3d}}, \text{ if } Fr \lesssim 1, \text{ and } |fW/U| \lesssim 1,$$

(46)

$$F_{\text{3d}} = C_2 h_0 W U^2, \quad \text{if } Fr \gg 1,$$

(47)

where similarly A_2, B_2 and C_2 are tunable constants, and F_{Bell3d} is as defined in (13). Our data gave the fitted values $A_2 = 1.34$, $B_2 = 0.88$ and $C_2 = 1$. Similar to (44), one could also change (46) to have a polynomial dependence on $|fW/U|$ if desired. Such an alternate form of (46) could be useful in the regime $A_2 - B_2|fW/U| \approx 0$, in which (46) is unphysical.

c. Suggested mixed flow parametrisations

For a mixed flow

$$U(t) = U_{\text{mean}} + U_{\text{tidal}} \cos(\omega t), \qquad (48)$$

with associated stress (parallel to $U(t)$)

$$F_{2d} = F_m + F_p \cos(\omega t + \phi), \qquad \text{(two dimensions)}$$
$$F_{3d} = F_m + F_p \cos(\omega t + \phi), \qquad \text{(three dimensions)}$$

the naive parametrisation

$$F_m = \widetilde{F}_m, \qquad F_p = \widetilde{F}_p \qquad (49)$$

proved to be accurate for a wide range of parameters. Here, as in Sections 4e and 4f, $\widetilde{F}_m$ and $\widetilde{F}_p$ are the values of F_m and F_p if U_{tidal} or U_{mean} are set to be zero respectively. In two dimensions, the main regimes where (49) disagreed with, and notably underestimated, our simulation output were those near the critical latitude $|f| = \omega$, those with small values of U_{mean} (for F_m), and those with small values for W (for F_p). Then, in three dimensions, the naive parametrisation again underestimated the simulation data near the critical latitude $|f| = \omega$ (for F_p), and also for large hill heights h_0 (for F_m). For this last point, we suggest setting

$$F_m = \widetilde{F}_m \left(1 + \frac{U_{\text{tidal}}^2}{2U_{\text{mean}}^2}\right), \qquad (50)$$

in three dimensions whenever the Froude number $Fr = Nh_0/U_{\text{mean}}$ is large. The formula (50) is derived from the quadratic drag law (47) we observed in the steady flow case for $Fr \gg 1$. However, as discussed in Section 4f, it would be preferable to do more tests and analysis to evaluate the accuracy of (50), and to better understand the transition between the low and high Froude number regimes.

In the bottom-trapped regime ($|f| > \omega$), the phase ϕ also notably disagreed with that predicted by the Shakespeare et al. (2020) theory for tidal flows, but still satisfied $\phi \approx 0$ for $|f| \ll \omega$.

6. Conclusion

We have evaluated common stress parametrisations for tidal, steady and mixed flows over rough topography. In the case where the topography is an isolated Gaussian hill in two or three dimensions, we have directly compared these parametrisations with idealised numerical simulations. This helped clarify the cases for which the parametrisations and simulations agreed and disagreed. We found that the most notable regimes where the parametrisations and simulations disagreed were (i) when the topographic height h_0 was large, and (ii), when the magnitude of the Coriolis parameter $|f|$ was close to the tidal frequency ω (for tidal and mixed flows). This was not entirely unexpected, as the existing parametrisations were often designed for small hill heights h_0 or in the case where $|f| \ll \omega$.

We also suggested simple adjustments or new parametrisations in the cases where the existing theory falls short. In most cases, only simple adjustments to the standard theory was required, highlighting the relative success of the underlying linear theory, even in regimes considered to be strongly non-linear. It is hoped that these updated parametrisations may be used to more accurately model stress in regimes for which there is currently limited theory available. However, before applying our work to large-scale ocean models, there are some notable limitations that need further consideration.

Firstly, one would need to test how well our scalings and parametrisations hold with more complicated topography, beyond the isolated hill scenario that we studied. For example, as we mentioned in the text, Klymak et al. (2021) found that for steady flows in three-dimensions, the stress varies differently with the buoyancy frequency N depending on whether one has an isolated obstacle, or multiple randomly distributed obstacles. Our assumption that N is uniform should also be relaxed, and as discussed by Lüschow and Von Storch (2024), the choice of N that one uses in a parametrisation can significantly affect the accuracy of the model.

Secondly, there are some specific parameter regimes where more analysis is needed. In particular, more investigation is needed of steady flow regimes where the Froude number Fr has an intermediate value, rather than just the limits $Fr \lesssim 1$ and $Fr \gg 1$ considered here.

Lastly, a critical step in implementing any stress parameterisation is determining where in the vertical the stress should be applied to the flow, which was not considered here. However, previous studies have provided guidance on this point. For mean stress, the propagating wave component is applied where the lee waves break and dissipate (e.g., Booker and Bretherton 1967; Andrews and Mcintyre 1976; Xie and Vanneste 2015), while the non-propagating part acts directly adjoining the hill (e.g., Klymak et al. 2010; Klymak 2018; Klymak et al. 2021). By contrast, for periodic stress, the force acts in the diffusive boundary layer adjoining the topography as shown in Shakespeare et al. (2021a). However, no previous studies have considered the mixed flow case, in which this picture may differ, and this is clearly an important avenue for further investigation.

Despite these limitations, the present work provides an important step towards a more comprehensive and robust parametrisation of topographic stresses in ocean models.

and John Scinocca for sharing their thoughts on an early draft of this paper at the CCCma in Victoria, Canada during June 2024. N.C.C. acknowledges support from the Australian Research Council under DECRA Fellowship DE210100749, Discovery Project DP240101274, and the Center of Excellence for the Weather of the 21st Century CE230100012.

References

Aguilar, D. A., and B. R. Sutherland, 2006: Internal wave generation from rough topography. *Physics of Fluids*, **18 (6)**.

Andrews, D. G., and M. E. Mcintyre, 1976: Planetary waves in horizontal and vertical shear: The generalized Eliassen-Palm relation and the mean zonal acceleration. *Journal of Atmospheric Sciences*, **33 (11)**, 2031–2048.

Ansong, J. K., B. K. Arbic, M. C. Buijsman, J. G. Richman, J. F. Shriver, and A. J. Wallcraft, 2015: Indirect evidence for substantial damping of low-mode internal tides in the open ocean. *Journal of Geophysical Research: Oceans*, **120 (9)**, 6057–6071.

Arbic, B. K., O. B. Fringer, J. M. Klymak, F. T. Mayer, D. S. Trossman, and P. Zhu, 2019: Connecting process models of topographic wave drag to global eddying general circulation models. *Oceanography*, **32 (4)**, 146–155.

Arbic, B. K., and Coauthors, 2018: Primer on global internal tide and internal gravity wave continuum modeling in HYCOM and MITgcm. *New Frontiers in Operational Oceanography*, 307–392.

Baker, L. E., and A. Mashayek, 2022: The impact of representations of realistic topography on parameterized oceanic lee wave energy flux. *Journal of Geophysical Research: Oceans*, **127 (10)**, e2022JC018 995.

Balmforth, N. J., G. R. Ierley, and W. R. Young, 2002: Tidal conversion by subcritical topography. *Journal of Physical Oceanography*, **32 (10)**, 2900–2914.

Bell, T. H., 1975: Topographically generated internal waves in the open ocean. *Journal of Geophysical Research*, **80 (3)**, 320–327.

Booker, J. R., and F. P. Bretherton, 1967: The critical layer for internal gravity waves in a shear flow. *Journal of fluid mechanics*, **27 (3)**, 513–539.

Buijsman, M. C., B. K. Arbic, J. Green, R. W. Helber, J. G. Richman, J. F. Shriver, P. Timko, and A. Wallcraft, 2015: Optimizing internal wave drag in a forward barotropic model with semidiurnal tides. *Ocean Modelling*, **85**, 42–55.

Clark, M. R., and Coauthors, 2010: The ecology of seamounts: structure, function, and human impacts. *Annual Review of Marine Science*, **2**, 253–278.

Cusack, J. M., J. A. Brearley, A. C. Naveira G., D. A. Smeed, K. L. Polzin, N. Velzeboer, and C. J. Shakespeare, 2020: Observed eddy–internal wave interactions in the southern ocean. *Journal of Physical Oceanography*, **50 (10)**, 3043–3062.

de Lavergne, C., S. Falahat, G. Madec, F. Roquet, J. Nycander, and C. Vic, 2019: Toward global maps of internal tide energy sinks. *Ocean Modelling*, **137**, 52–75.

Eden, C., D. Olbers, and T. Eriksen, 2021: A closure for lee wave drag on the large-scale ocean circulation. *Journal of Physical Oceanography*, **51 (12)**, 3573–3588.

Egbert, G. D., and R. D. Ray, 2000: Significant dissipation of tidal energy in the deep ocean inferred from satellite altimeter data. *Nature*, **405 (6788)**, 775–778.

Egbert, G. D., and R. D. Ray, 2001: Estimates of M2 tidal energy dissipation from topex/poseidon altimeter data. *Journal of Geophysical Research: Oceans*, **106 (C10)**, 22 475–22 502.

Falahat, S., and J. Nycander, 2015: On the generation of bottom-trapped internal tides. *Journal of Physical Oceanography*, **45 (2)**, 526–545.

Garner, S. T., 2005: A topographic drag closure built on an analytical base flux. *Journal of the Atmospheric Sciences*, **62 (7)**, 2302–2315.

Garrett, C., and E. Kunze, 2007: Internal tide generation in the deep ocean. *Annu. Rev. Fluid Mech.*, **39**, 57–87.

Geoffroy, G., F. Pollmann, and J. Nycander, 2024: Tidal conversion into vertical normal modes by near-critical topography. *Journal of Physical Oceanography*, **54 (9)**, 1949–1970.

Green, J. A. M., and J. Nycander, 2013: A comparison of tidal conversion parameterizations for tidal models. *Journal of Physical Oceanography*, **43 (1)**, 104–119.

Harris, P. T., M. Macmillan-Lawler, J. Rupp, and E. K. Baker, 2014: Geomorphology of the oceans. *Marine Geology*, **352**, 4–24.

Jayne, S. R., 2009: The impact of abyssal mixing parameterizations in an ocean general circulation model. *Journal of Physical Oceanography*, **39 (7)**, 1756–1775.

Jayne, S. R., and L. C. St. Laurent, 2001: Parameterizing tidal dissipation over rough topography. *Geophysical Research Letters*, **28 (5)**, 811–814.

Johnston, D. R., N. C. Constantinou, and J. Shakespeare, Callum, 2025: ocean-hill-stress v0.1.0. Zenodo, URL https://doi.org/10.5281/zenodo.17274188, doi:10.5281/zenodo.17274188.

Khatiwala, S., 2003: Generation of internal tides in an ocean of finite depth: analytical and numerical calculations. *Deep Sea Research Part I: Oceanographic Research Papers*, **50 (1)**, 3–21.

Kiss, A. E., and Coauthors, 2020: ACCESS-OM2 v1.0: a global ocean–sea ice model at three resolutions. *Geoscientific Model Development*, **13 (2)**, 401–442.

Klymak, J. M., 2018: Nonpropagating form drag and turbulence due to stratified flow over large-scale abyssal hill topography. *Journal of Physical Oceanography*, **48 (10)**, 2383–2395.

Klymak, J. M., D. Balwada, A. N. Garabato, and R. Abernathey, 2021: Parameterizing nonpropagating form drag over rough bathymetry. *Journal of Physical Oceanography*, **51 (5)**, 1489–1501.

Klymak, J. M., S. M. Legg, and R. Pinkel, 2010: High-mode stationary waves in stratified flow over large obstacles. *Journal of Fluid Mechanics*, **644**, 321–336.

Ledwell, J. R., E. T. Montgomery, K. L. Polzin, L. C. St. Laurent, R. W. Schmitt, and J. M. Toole, 2000: Evidence for enhanced mixing over rough topography in the abyssal ocean. *Nature*, **403 (6766)**, 179–182.

Legg, S., and K. M. H. Huijts, 2006: Preliminary simulations of internal waves and mixing generated by finite amplitude tidal flow over isolated topography. *Deep Sea Research Part II: Topical Studies in Oceanography*, **53 (1-2)**, 140–156.

Llewellyn Smith, S. G., and W. R. Young, 2002: Conversion of the barotropic tide. *Journal of Physical Oceanography*, **32 (5)**, 1554–1566.

Lott, F., and M. J. Miller, 1997: A new subgrid-scale orographic drag parametrization: Its formulation and testing. *Quarterly Journal of the Royal Meteorological Society*, **123 (537)**, 101–127.

Lüschow, V., and J. Von Storch, 2024: Sensitivity of internal-tide generation to stratification and its implication for deep overturning circulations. *Journal of Physical Oceanography*, **54 (1)**, 319–330.

Maitland-Davies, C., and O. Bühler, 2025: Oceanic Lee Waves in a Linearly Sheared Flow. *Journal of Physical Oceanography*, **55 (5)**, 543–558.

Melet, A., R. Hallberg, S. Legg, and M. Nikurashin, 2014: Sensitivity of the ocean state to lee wave–driven mixing. *Journal of Physical Oceanography*, **44 (3)**, 900–921.

Melet, A., R. Hallberg, S. Legg, and K. Polzin, 2013: Sensitivity of the ocean state to the vertical distribution of internal-tide-driven mixing. *Journal of Physical Oceanography*, **43 (3)**, 602–615.

Munk, W., and C. Wunsch, 1998: Abyssal recipes II: Energetics of tidal and wind mixing. *Deep Sea Research Part I: Oceanographic Research Papers*, **45 (12)**, 1977–2010.

Naveira Garabato, A. C., A. J. G. Nurser, R. B. Scott, and J. A. Goff, 2013: The impact of small-scale topography on the dynamical balance of the ocean. *Journal of Physical Oceanography*, **43 (3)**, 647–668.

Nikurashin, M., R. Ferrari, N. Grisouard, and K. Polzin, 2014: The impact of finite-amplitude bottom topography on internal wave generation in the Southern Ocean. *Journal of Physical Oceanography*, **44 (11)**, 2938–2950.

Nycander, J., 2005: Generation of internal waves in the deep ocean by tides. *Journal of Geophysical Research: Oceans*, **110 (C10)**.

Olbers, D., and C. Eden, 2013: A global model for the diapycnal diffusivity induced by internal gravity waves. *Journal of Physical Oceanography*, **43 (8)**, 1759–1779.

Peltier, W. R., and T. L. Clark, 1979: The evolution and stability of finite-amplitude mountain waves. Part II: Surface wave drag and severe downslope windstorms. *Journal of Atmospheric Sciences*, **36 (8)**, 1498–1529.

Perfect, B., N. Kumar, and J. J. Riley, 2020: Energetics of seamount wakes. Part II: Wave fluxes. *Journal of Physical Oceanography*, **50 (5)**, 1383–1398.

Pollmann, F., and J. Nycander, 2023: Resolving the horizontal direction of internal tide generation: Global application for the m 2 tide's first mode. *Journal of Physical Oceanography*, **53 (5)**, 1251–1267.

Pressel, K. G., S. Mishra, T. Schneider, C. M. Kaul, and Z. Tan, 2017: Numerics and subgrid-scale modeling in large eddy simulations of stratocumulus clouds. *J. Adv. Model. Earth Syst.*, **9 (2)**, 1342–1365.

Ramadhan, A., and Coauthors, 2020: Oceananigans.jl: Fast and friendly geophysical fluid dynamics on GPUs. *Journal of Open Source Software*, **5 (53)**, 2018, doi:10.21105/joss.02018.

Sandstrom, H., and J. A. Elliott, 1984: Internal tide and solitons on the Scotian Shelf: A nutrient pump at work. *Journal of Geophysical Research: Oceans*, **89 (C4)**, 6415–6426.

Scinocca, J. F., and N. A. McFarlane, 2000: The parametrization of drag induced by stratified flow over anisotropic orography. *Quarterly Journal of the Royal Meteorological Society*, **126 (568)**, 2353–2393.

Shakespeare, C. J., 2020: Interdependence of internal tide and lee wave generation at abyssal hills: Global calculations. *Journal of Physical Oceanography*, **50 (3)**, 655–677.

Shakespeare, C. J., B. K. Arbic, and A. M. Hogg, 2020: The drag on the barotropic tide due to the generation of baroclinic motion. *Journal of Physical Oceanography*, **50 (12)**, 3467–3481.

Shakespeare, C. J., B. K. Arbic, and A. M. Hogg, 2021a: The impact of abyssal hill roughness on the benthic tide. *Journal of Advances in Modeling Earth Systems*, **13 (5)**, e2020MS002 376.

Shakespeare, C. J., B. K. Arbic, and A. McC. Hogg, 2021b: Dissipating and reflecting internal waves. *Journal of Physical Oceanography*, **51 (8)**, 2517–2531.

Shchepetkin, A. F., and J. C. McWilliams, 2005: The regional oceanic modeling system (roms): a split-explicit, free-surface, topography-following-coordinate oceanic model. *Ocean Modelling*, **9 (4)**, 347–404, doi:10.1016/j.ocemod.2004.08.002.

Shu, C.-W., 2020: Essentially non-oscillatory and weighted essentially non-oscillatory schemes. *Acta Numer.*, **29**, 701–762.

Silvestri, S., G. L. Wagner, J.-M. Campin, N. C. Constantinou, C. N. Hill, A. Souza, and R. Ferrari, 2024: A new WENO-based momentum advection scheme for simulations of ocean mesoscale turbulence. *J. Adv. Model. Earth Sy.*, **16 (7)**, e2023MS004 130.

Silvestri, S., and Coauthors, 2025: A GPU-based ocean dynamical core for routine mesoscale-resolving climate simulations. *J. Adv. Model. Earth Sy.*, **17**, e2024MS004 465, doi:10.1029/2024MS004465.

Simmons, H. L., S. R. Jayne, L. C. S. Laurent, and A. J. Weaver, 2004: Tidally driven mixing in a numerical model of the ocean general circulation. *Ocean Modelling*, **6 (3-4)**, 245–263.

Trossman, D. S., B. K. Arbic, S. T. Garner, J. A. Goff, S. R. Jayne, E. J. Metzger, and A. J. Wallcraft, 2013: Impact of parameterized lee wave drag on the energy budget of an eddying global ocean model. *Ocean Modelling*, **72**, 119–142.

Trossman, D. S., B. K. Arbic, J. G. Richman, S. T. Garner, S. R. Jayne, and A. J. Wallcraft, 2016: Impact of topographic internal lee wave drag on an eddying global ocean model. *Ocean Modelling*, **97**, 109–128.

Trossman., D. S., S. Waterman, K. L. Polzin, B. K. Arbic, S. T. Garner, A. C. Naveira-Garabato, and K. L. Sheen, 2015: Internal lee wave closures: Parameter sensitivity and comparison to observations. *Journal of Geophysical Research: Oceans*, **120 (12)**, 7997–8019.

Wagner, G. L., and Coauthors, 2025: High-level, high-resolution ocean modeling at all scales with Oceananigans. *arXiv preprint*, doi:10.48550/arXiv.2502.14148, 2502.14148.

Watts, A., 2019: Science, seamounts and society. *Geoscientist*, **290 (7)**, 10–16.

Winters, K. B., and L. Armi, 2014: Topographic control of stratified flows: Upstream jets, blocking and isolating layers. *Journal of Fluid Mechanics*, **753**, 80–103.

Xie, J.-H., and J. Vanneste, 2015: A generalised-Lagrangian-mean model of the interactions between near-inertial waves and mean flow. *Journal of Fluid Mechanics*, **774**, 143–169.

Zarroug, M., J. Nycander, and K. Döös, 2010: Energetics of tidally generated internal waves for nonuniform stratification. *Tellus A: Dynamic Meteorology and Oceanography*, **62 (1)**, 71–79.

Zemskova, V. E., and N. Grisouard, 2022: Energetics and mixing of stratified, rotating flow over abyssal hills. *Journal of Physical Oceanography*, **52 (6)**, 1155–1177.